aerospace

MDPI

Article

Hierarchical Coupling/Disturbance-Utilization Control for Tiltable Quadrotors

Tiancai Wu [1,2], Jie Bai [1,3,*] and Min Xiong [4]

[1] Hangzhou City University Binjiang Innovation Center, Hangzhou 310051, China; wutic@buaa.edu.cn
[2] College of Information Science and Electronic Engineering, Zhejiang University, Hangzhou 310027, China
[3] Intelligent Transportation System Research Center, Hangzhou City University, Hangzhou 310015, China
[4] R&D Department, Jiangxi Jiangling Group Electric Vehicle Co., Ltd., Nanchang 330114, China; xiongm@jmev.com
* Correspondence: baij@hzcu.edu.cn

Abstract

Tiltable quadrotors have the ability of independent control of position and attitude, which can be more flexible in complex task scenarios. However, the inherent unmodeled dynamics, model uncertainties, and external disturbances pose significant challenges to the control system design. Aiming at the the control problem of tiltable quadrotors, this paper proposes a hierarchical adaptive coupling/disturbance utilization control strategy. First, an error-dynamics model is developed, explicitly incorporating coupling effects and lumped disturbances. Then, hierarchical adaptive coupling/disturbance utilization mechanisms are designed to adaptively exploit coupling and disturbances to improve system performance. Subsequently, super-twisting higher-order sliding-mode observers and robust tracking control laws are synthesized to estimate lumped disturbances and guarantee system robustness. Finally, through theoretical analysis, the stability of the closed-loop system and the role of hierarchical adaptive coupling/disturbance utilization mechanisms are elucidated. The effectiveness of the proposed control strategy is validated through simulations and flight experiments.

Keywords: tiltable quadrotors; anti-disturbance control; coupling/disturbance utilization; independent control of position and attitude

1. Introduction

Quadrotors, due to their high maneuverability and operational simplicity, are widely used in applications such as aerial photography, delivery, and inspection [1–4]. However, the coplanar rotor structure means that thrust can only be generated perpendicularly to the body, resulting in system underactuation (i.e., translation and rotational motions influence each other). This underactuation characteristic severely limits the deployment of quadrotors in complex scenarios, such as navigation or physical interaction tasks in confined spaces [5].

To overcome this limitation, tiltable quadrotors have received considerable attention. By designing servo and rotation mechanisms, the rotor planes of tiltable quadrotors can be actively tilted, thereby generating a three-dimensional thrust vector and enabling independent position and attitude control [6,7]. However, the resulting model uncertainties, unmodeled dynamics, and complex disturbances pose significant challenges to control system design [8].

Check for updates

Received: 16 January 2026
Revised: 4 March 2026
Accepted: 11 March 2026
Published: 12 March 2026

Copyright: © 2026 by the authors. Licensee MDPI, Basel, Switzerland. This article is an open access article distributed under the terms and conditions of the Creative Commons Attribution (CC BY) license.

In recent years, several representative studies have investigated the control of tiltable quadrotors. The development of these approaches has evolved from linear control schemes to nonlinear strategies, and further toward disturbance rejection frameworks. Based on classical control theory, Özdoğan et al. linearized the tiltable quadrotor dynamics around an equilibrium point and subsequently designed a proportional–integral–derivative controller using the "manual loop shaping" method to achieve the desired frequency-domain characteristics of the closed-loop system [9]. However, such linearization-based methods are inherently sensitive to operating-point variations, and performance degradation is often observed when the state of the system is perturbed from equilibrium. To better address system nonlinearities, based on feedback linearization techniques, Ryll et al. developed independent position and attitude control laws [7]. In [10], a decentralized backstepping control scheme is proposed by Saif et al., in which controller parameters are optimized using a differential evolution strategy. Shayan et al. introduced a nonlinear model predictive control (NMPC) method that explicitly accounts for feasible control allocation constraints [11]. To further enhance control performance and accelerate optimization convergence, Li et al. incorporated servo dynamics into the NMPC framework [12]. However, such methods typically rely on accurate models, and when deployed on real-world tiltable quadrotor platforms, model uncertainties and external disturbances can affect their control performance. To improve the anti-disturbance capability of tiltable quadrotor control systems, techniques such as extended state observers (ESO) [13], disturbance observers (DO) [5], and neural network-based methods [14,15] have been developed to estimate lumped system disturbances, which are then actively compensated within the control law.

Despite their demonstrated effectiveness in simulations and experiments, most disturbance rejection control schemes rely on the assumption that lumped disturbances are always detrimental to closed-loop tracking, and thus adopt conservative full-compensation strategies. However, growing evidence suggests that this assumption is not universally valid and that properly exploiting disturbance information can even enhance control performance under certain conditions [16]. Several studies on disturbance utilization-based control have been demonstrated to be effective for systems such as permanent magnet synchronous motors [17], satellites [18,19], manned submersible vehicles [20], and hypersonic vehicles [21–23]. For example, in satellite systems subject to composite disturbances, Teng et al. employed a sliding-mode observer to estimate the lumped disturbances and subsequently introduced a disturbance discrimination operator to identify the nature of the disturbances, i.e., whether they are beneficial or harmful to the system performance. Based on this discrimination mechanism, a green control scheme was developed [18]. Similarly, Sun et al. employed an ESO to estimate disturbances acting on a hypersonic vehicle and designed a disturbance characteristic indicator to evaluate their effects on system performance, thereby constructing a conditional disturbance negation-based active disturbance rejection control framework, which was shown to outperform conventional disturbance rejection control methods [22]. Wu et al. were the first to explore disturbance utilization in tiltable quadrotor systems. Specifically, they employed an unknown system dynamics estimator (USDE) to estimate lumped disturbances and then established a flexible disturbance compensation control framework by integrating a disturbance characteristic indicator with a utilization mechanism [24]. However, this method only improves performance by utilizing disturbances in the inner loops (velocity loop and angular rate loop), without considering how to further enhance the performance of the outer loops (position loop and angle loop). In addition, the binary form of disturbance utilization may induce the chattering phenomenon.

Overall, there are still some key challenges in further applying the aforementioned disturbance utilization control techniques to tiltable quadrotors.

(1) The position and attitude subsystems of tiltable quadrotors are both second-order systems, where the outer loop corresponds to kinematics (position and attitude angle) and the inner loop corresponds to dynamics (velocity and angular velocity). Disturbances primarily exist in the inner loop. Existing disturbance utilization control schemes can effectively improve the performance of the inner loop, yet provide limited capability to adjust the performance of the outer loop. Therefore, it is necessary to investigate the coupling between the inner and outer loops and to exploit it to improve overall system performance.

(2) Most existing disturbance exploitation methods utilize beneficial disturbances and fully compensated harmful disturbances. However, utilizing the negative impacts of harmful interference can also enhance the system performance. In addition, disturbance characteristic indicators and utilization mechanisms based on binary decision logic can easily lead to system chattering. Therefore, it is necessary to develop an adaptive and smooth disturbance utilization mechanism.

To address the above issues, this paper proposes a hierarchical adaptive coupling/disturbance utilization control strategy for tiltable quadrotors. The main contributions of this paper are summarized as follows:

(1) A control-oriented error dynamics model is established for tiltable quadrotors, explicitly incorporating both inner–outer loop coupling and lumped disturbances. Based on this model, coupling and disturbance characteristic indices are developed, thereby laying the foundation for a hierarchical coupling/disturbance utilization control framework. Compared with existing results [18,21,24], this approach has the potential to further enhance overall control performance.

(2) Super-twisting sliding mode observers and robust tracking control laws are designed to improve the convergence speed of disturbance estimation and tracking error regulation, respectively. Compared with existing disturbance utilization control frameworks employing observers such as DO [5], ESO [13], and USDE [24], as well as backstepping- or dynamic-surface-based control laws [25,26], the deployed observers and control laws can theoretically achieve faster convergence.

(3) An adaptive coupling/disturbance utilization mechanism is developed. The proposed mechanism not only avoids the chattering phenomenon induced by traditional binary decision logic [17,20], but also enables a smooth exploitation of both beneficial couplings/disturbances and the negative of detrimental ones, thereby improving overall system performance.

The remainder of this paper is organized as follows. The problem formulation is given in Section 2. The proposed control scheme is designed in Section 3. Sections 4 and 5 give the simulation and experimental results, respectively. Finally, conclusions are drawn in Section 6.

2. Problem Formulation

2.1. Dynamics Model

The dynamic models of the position and attitude subsystems of the tiltable quadrotors, illustrated in Figure 1, are given as follows [13,24,27]:

$$\begin{cases} \dot{\boldsymbol{p}} = \boldsymbol{v}, \\ \dot{\boldsymbol{v}} = \boldsymbol{G}_v \boldsymbol{f}_a + \boldsymbol{f}_v + \boldsymbol{d}_v, \end{cases} \tag{1}$$

$$\begin{cases} \dot{\boldsymbol{\Omega}} = \boldsymbol{G}_\Omega \boldsymbol{\omega}, \\ \dot{\boldsymbol{\omega}} = \boldsymbol{G}_\omega \boldsymbol{\tau}_a + \boldsymbol{f}_\omega + \boldsymbol{d}_\omega, \end{cases} \tag{2}$$

https://doi.org/10.3390/aerospace13030269

where $\boldsymbol{p} = [x, y, z]^{\mathrm{T}}$ and $\boldsymbol{v} = [v_x, v_y, v_z]^{\mathrm{T}}$ are the position and velocity vectors, respectively; $\boldsymbol{\Omega} = [\phi, \theta, \psi]^{\mathrm{T}}$ and $\boldsymbol{\omega} = [p, q, r]^{\mathrm{T}}$ are the attitude angle and angular rate vectors, respectively. Here, ϕ, θ, and ψ represent the roll, pitch, and yaw angles, respectively, while p, q, and r represent the corresponding roll, pitch, and yaw angular rates. Moreover, $\boldsymbol{G}_v = \frac{1}{m}\boldsymbol{R}_b^e$, where m denotes the total mass of the vehicle and $\boldsymbol{R}_b^e$ represents the rotation matrix from the body frame to the inertial frame. In addition, $\boldsymbol{G}_\omega = \boldsymbol{J}_{b,a}^{-1}$, where $\boldsymbol{J}_{b,a}$ denotes the inertia matrix. The matrix $\boldsymbol{G}_\Omega$ is defined as:

$$\boldsymbol{G}_\Omega = \begin{bmatrix} 1 & \tan\theta\sin\phi & \tan\theta\cos\phi \\ 0 & \cos\phi & -\sin\phi \\ 0 & \dfrac{\sin\phi}{\cos\theta} & \dfrac{\cos\phi}{\cos\theta} \end{bmatrix}$$

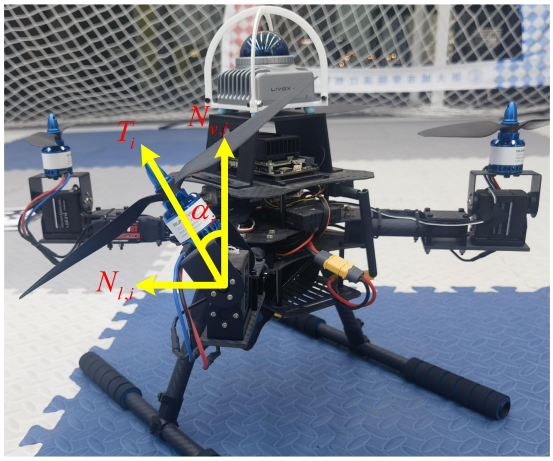


Figure 1. Tiltable quadrotor schematic and the relationship between the virtual and actual control inputs.

The model terms $\boldsymbol{f}_v$ and $\boldsymbol{f}_\omega$, together with the lumped disturbance terms $\boldsymbol{d}_v$ and $\boldsymbol{d}_\omega$, are given as:

$$\boldsymbol{f}_v = \boldsymbol{g} - \frac{1}{m}\boldsymbol{R}_b^e \sum_{i=1}^{4}\sum_{j=1}^{2} m_{ij}\left(\boldsymbol{\omega} \times \left(\boldsymbol{\omega} \times \boldsymbol{P}_{e,ij}\right)\right), \tag{3}$$

$$\boldsymbol{d}_v = \Delta\boldsymbol{G}_v\boldsymbol{f}_a + \Delta\boldsymbol{f}_v - \frac{1}{m}\boldsymbol{R}_b^e \sum_{i=1}^{4}\sum_{j=1}^{2} m_{ij}\left(\ddot{\boldsymbol{p}}_{e,ij} + 2\boldsymbol{\omega} \times \dot{\boldsymbol{p}}_{e,ij} + \dot{\boldsymbol{\omega}} \times \boldsymbol{p}_{e,ij}\right) + \boldsymbol{d}_{v,ex}, \tag{4}$$

$$\boldsymbol{f}_\omega = \boldsymbol{J}_{b,a}^{-1}\left[\sum_{i=1}^{4}\sum_{j=1}^{2}\left(\boldsymbol{p}_{e,ij} \times m_{ij}\boldsymbol{R}_e^b\boldsymbol{g}\right) - \boldsymbol{\omega} \times \boldsymbol{J}_b\boldsymbol{\omega}\right], \tag{5}$$

$$\boldsymbol{d}_\omega = \Delta\boldsymbol{G}_\omega\boldsymbol{\tau}_a + \Delta\boldsymbol{f}_\omega - \boldsymbol{J}_{b,a}^{-1}\sum_{i=1}^{4}\sum_{j=1}^{2}\left(\boldsymbol{J}_{ij}\left(\dot{\boldsymbol{\omega}}_{r,ij} + \boldsymbol{\omega} \times \boldsymbol{\omega}_{r,ij}\right) + \left(\boldsymbol{\omega} + \boldsymbol{\omega}_{r,ij}\right) \times \boldsymbol{J}_{ij}\left(\boldsymbol{\omega} + \boldsymbol{\omega}_{r,ij}\right) + \boldsymbol{p}_{e,ij} \times \boldsymbol{f}_{e,ij}\right) + \boldsymbol{d}_{\omega,ex}, \tag{6}$$

where $\Delta\boldsymbol{G}_v\boldsymbol{f}_a$, $\Delta\boldsymbol{f}_v$, $\Delta\boldsymbol{G}_\omega\boldsymbol{\tau}_a$, and $\Delta\boldsymbol{f}_\omega$ represent inherent model uncertainties, while $\boldsymbol{d}_{v,ex}$ and $\boldsymbol{d}_{\omega,ex}$ denote external disturbances.

The control force $\boldsymbol{f}_a$ and control torque $\boldsymbol{\tau}_a$ are given by:

$$\begin{bmatrix} \boldsymbol{f}_a \\ \boldsymbol{\tau}_a \end{bmatrix} = \boldsymbol{A}\boldsymbol{N} \tag{7}$$

where $\boldsymbol{A}$ denotes the control effectiveness matrix and

$$\boldsymbol{N} = [N_{l,1},\ N_{v,1},\ N_{l,2},\ N_{v,2},\ N_{l,3},\ N_{v,3},\ N_{l,4},\ N_{v,4}]^{\mathrm{T}}$$

is the vector of virtual control inputs. The relationship between the virtual control inputs $N_{l,i}$ and $N_{v,i}$ and the actual control inputs n_i and α_i of the tiltable quadrotor is given by:

$$\begin{cases} N_{v,i} = T_i \cos(\alpha_i), \\ N_{l,i} = T_i \sin(\alpha_i), \end{cases} \tag{8}$$

where $i = 1, 2, 3, 4$, $T_i = c_T n_i^2$ denotes the thrust generated by the i-th rotor, c_T is the thrust coefficient, n_i denotes the rotational speed, and α_i denotes the tilting angle of the i-th servo. For brevity, the definitions of the remaining symbols can be found in [24].

Assumption 1. *To avoid the singularity, the pitch angle θ is assumed to be constrained within the range of $(-\frac{\pi}{2}, \frac{\pi}{2})$.*

Assumption 2. *The lumped disturbances $\boldsymbol{d}_v$ and $\boldsymbol{d}_\omega$ and their time derivatives are bounded, i.e., there exist positive constants D_v, L_v, D_ω and L_ω, such that $\|\boldsymbol{d}_v\| \leq D_v$, $\|\dot{\boldsymbol{d}}_v\| \leq L_v$, $\|\boldsymbol{d}_\omega\| \leq D_\omega$, and $\|\dot{\boldsymbol{d}}_\omega\| \leq L_\omega$.*

Remark 1. *In aircraft control, it is common and reasonable to assume that the lumped disturbance and its time derivative are bounded. This is because the lumped disturbance typically comprises wind, airflow effects, unmodeled dynamics, and modeling uncertainties, which are continuous over any finite time interval.*

2.2. Control-Oriented Error Dynamics

As shown in Equations (1) and (2), both the position and attitude subsystems of the tiltable quadrotor are second-order systems. To facilitate the design of the hierarchical coupling/disturbance-utilization control architecture, and inspired by the modeling method in [25], the following error dynamics models are defined as:

$$\begin{cases} \dot{\boldsymbol{e}}_p = \boldsymbol{e}_v + \boldsymbol{v}_c - \dot{\boldsymbol{p}}_c, \\ \dot{\boldsymbol{e}}_v = \boldsymbol{G}_v \boldsymbol{f}_a + \boldsymbol{f}_v + \boldsymbol{d}_v - \dot{\boldsymbol{v}}_c, \end{cases} \tag{9}$$

$$\begin{cases} \dot{\boldsymbol{e}}_\Omega = \bar{\boldsymbol{G}}_\Omega \boldsymbol{e}_\omega + \bar{\boldsymbol{G}}_\Omega \boldsymbol{w}_c + \boldsymbol{f}_\Omega - \dot{\boldsymbol{\Omega}}_c, \\ \dot{\boldsymbol{e}}_\omega = \boldsymbol{G}_\omega \boldsymbol{\tau}_a + \boldsymbol{f}_\omega + \boldsymbol{d}_\omega - \dot{\boldsymbol{\omega}}_c, \end{cases} \tag{10}$$

where $\boldsymbol{e}_p = \boldsymbol{p} - \boldsymbol{p}_c$ and $\boldsymbol{e}_v = \boldsymbol{v} - \boldsymbol{v}_c$ denote position and velocity tracking errors, respectively; $\boldsymbol{e}_\Omega = \boldsymbol{\Omega} - \boldsymbol{\Omega}_c$ and $\boldsymbol{e}_\omega = \boldsymbol{\omega} - \boldsymbol{\omega}_c$ denote attitude angle and angular rate tracking errors, respectively; $\boldsymbol{p}_c$, $\boldsymbol{v}_c$, $\boldsymbol{\Omega}_c$, and $\boldsymbol{\omega}_c$ represent the desired commands; $\bar{\boldsymbol{G}}_\Omega = \mathrm{diag}\left\{1, \cos\phi, \frac{\cos\phi}{\cos\theta}\right\}$; $\boldsymbol{f}_\Omega = [q\tan\theta\sin\phi + r\tan\theta\cos\phi, -r\sin\phi, q\frac{\sin\phi}{\cos\theta}]^{\mathrm{T}}$.

Remark 2. *In this paper, the considered coupling refers to the state coupling between the inner and outer control loops. Taking Equation (9) as an example, the term $\boldsymbol{e}_v$ in the position tracking error dynamics $\dot{\boldsymbol{e}}_p$ represents the state coupling induced by the velocity control loop. Regarding such coupling effects, as well as the disturbances $\boldsymbol{d}_v$ and $\boldsymbol{d}_\omega$ appearing in the system dynamics, most existing control methods either neglect their influence or fully compensate for them to guarantee Lyapunov stability. In contrast, by designing coupling/disturbance characteristic indices and adaptive utilization mechanisms, this paper explicitly exploits these couplings and disturbances to further enhance system performance.*

3. Controller Design

The proposed control framework consists of two subsystems, each of which adopts a two-layer cascaded architecture, as illustrated in Figure 2. In the inner loops, super-twisting sliding-mode observers (ST-SMOs) are employed to estimate the lumped disturbances. Based on the estimated disturbances and the tracking errors of both the inner and outer loops, coupling/disturbance adaptive utilization mechanisms (C/D-AUMs) are developed. Subsequently, robust tracking control (RTC) laws are constructed using the tracking errors together with the outputs of the C/D-AUMs and ST-SMOs. In addition, to avoid the differential explosion problem, the desired commands generated by the outer-loop controllers are passed through first-order filters, and the filtered signals, along with their derivatives, are used as the reference inputs for the inner-loop controllers. Finally, after the desired forces and torques are obtained, control allocation and inverse mapping are performed to generate the actual control inputs for the tiltable quadrotor.

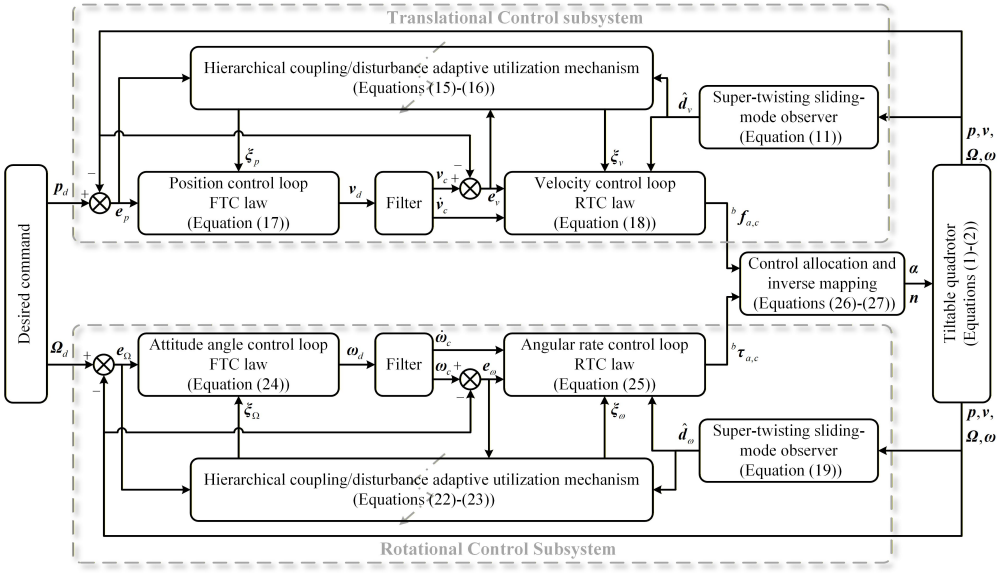


Figure 2. Architecture of the proposed hierarchical adaptive coupling/disturbance utilization control.

3.1. Translational Control Subsystem

3.1.1. ST-SMO Design

To estimate the disturbances present in the translational dynamics described in (1), the ST-SMO is constructed as [28]:

$$\begin{cases} \dot{\hat{\boldsymbol{v}}} = \boldsymbol{G}_v \boldsymbol{f}_a + \boldsymbol{f}_v - L_v^{1/2} \boldsymbol{\lambda}_{v,1} \mathbf{sig}^{1/2}(\hat{\boldsymbol{v}} - \boldsymbol{v}) + \hat{\boldsymbol{d}}_v, \\ \dot{\hat{\boldsymbol{d}}}_v = -L_v \boldsymbol{\lambda}_{v,2} \mathbf{sgn}(\hat{\boldsymbol{v}} - \boldsymbol{v}), \end{cases} \tag{11}$$

where $\hat{\boldsymbol{v}}$ and $\hat{\boldsymbol{d}}_v$ denote the estimates of $\boldsymbol{v}$ and $\boldsymbol{d}_v$, respectively; $\boldsymbol{\lambda}_{v,1} = \mathrm{diag}\{\lambda_{v,11}, \lambda_{v,12}, \lambda_{v,13}\}$ and $\boldsymbol{\lambda}_{v,2} = \mathrm{diag}\{\lambda_{v,21}, \lambda_{v,22}, \lambda_{v,23}\}$ denote the positive observer parameters; $\mathbf{sig}^{1/2}(\hat{\boldsymbol{v}} - \boldsymbol{v}) = [|\hat{v}_x - v_x|^{1/2}\,\mathrm{sgn}(\hat{v}_x - v_x), |\hat{v}_y - v_y|^{1/2}\,\mathrm{sgn}(\hat{v}_y - v_y), |\hat{v}_z - v_z|^{1/2}\,\mathrm{sgn}(\hat{v}_z - v_z)]^{\mathrm{T}}$; $\mathrm{sgn}(\cdot)$ denotes the sign function.

By defining the state estimation error $\tilde{\boldsymbol{v}} = \hat{\boldsymbol{v}} - \boldsymbol{v}$ and the disturbance estimation error $\tilde{\boldsymbol{d}}_v = \hat{\boldsymbol{d}}_v - \boldsymbol{d}_v$, the estimation error dynamics of the ST-SMO can be expressed as

$$\begin{cases} \dot{\tilde{\boldsymbol{v}}} = -L_v^{1/2} \boldsymbol{\lambda}_{v,1} \mathbf{sig}^{1/2}(\tilde{\boldsymbol{v}}) + \tilde{\boldsymbol{d}}_v, \\ \dot{\tilde{\boldsymbol{d}}}_v = -L_v \boldsymbol{\lambda}_{v,2} \mathbf{sgn}(\tilde{\boldsymbol{v}}) - \dot{\boldsymbol{d}}_v, \end{cases} \tag{12}$$

As can be seen from (12), the error dynamics are in the standard super-twisting form. Therefore, by applying Theorem 3 in [29], it follows that the state estimation error $\tilde{v}$ and the disturbance estimation error $\tilde{\boldsymbol{d}}_v$ converge to the origin in finite time. The detailed proof can be found in Theorem 3 of [29] and its associated derivation. Since finite-time convergence for the standard super-twisting form is well established in the literature, it is omitted here for brevity.

3.1.2. C/D-AUM Design

Motivated by [25] and guided by Lyapunov stability analysis, the coupling characteristic indices $\boldsymbol{J}_p = [J_{p,1}, J_{p,2}, J_{p,3}]^{\mathrm{T}}$ and the disturbance characteristic indices $\boldsymbol{J}_v = [J_{v,1}, J_{v,2}, J_{v,3}]^{\mathrm{T}}$ are defined as:

$$J_{p,i} = \begin{cases} 1, & \operatorname{sgn}(e_{p,i}e_{v,i}) \geq 0, \\ 0, & \operatorname{sgn}(e_{p,i}e_{v,i}) < 0, \end{cases} \tag{13}$$

$$J_{v,i} = \begin{cases} 1, & \operatorname{sgn}(e_{v,i}\hat{d}_{v,i}) \geq 0, \\ 0, & \operatorname{sgn}(e_{v,i}\hat{d}_{v,i}) < 0, \end{cases} \tag{14}$$

where $i = 1, 2, 3$ denotes the three channels of the translational dynamics. Specifically, taking $J_{p,i}$ as an example, $J_{p,i} \geq 0$ indicates that the coupling component $e_{v,i}$ negatively impacts tracking performance of $e_{p,i}$, whereas $J_{p,i} < 0$ implies that the coupling component contributes beneficially. For convenience, the special critical case $\operatorname{sgn}(e_{p,i}e_{v,i}) = 0$ is grouped together with the case $\operatorname{sgn}(e_{p,i}e_{v,i}) > 0$.

To avoid the chattering phenomenon induced by the binary-form characteristic indices in (13) and (14), the hierarchical coupling/disturbance adaptive utilization mechanisms $\boldsymbol{\xi}_p = [\xi_{p,1}, \xi_{p,2}, \xi_{p,3}]^{\mathrm{T}}$ and $\boldsymbol{\xi}_v = [\xi_{v,1}, \xi_{v,2}, \xi_{v,3}]^{\mathrm{T}}$ are designed as:

$$\xi_{p,i} = c_{p,1i} \tanh(\eta_{p,i}|e_{p,i}|) \operatorname{sgn}(e_{p,i}e_{v,i}) + \left(1 - c_{p,2i} \tanh(\eta_{p,i}|e_{p,i}|)\right), \tag{15}$$

$$\xi_{v,i} = c_{v,1i} \tanh(\eta_{v,i}|e_{v,i}|) \operatorname{sgn}(e_{v,i}\hat{d}_{v,i}) + \left(1 - c_{v,2i} \tanh(\eta_{v,i}|e_{v,i}|)\right), \tag{16}$$

where $\tanh(\cdot)$ denotes the hyperbolic tangent function; $c_{j,1i} > c_{j,2i} > 0$, and $\eta_{j,i} > 0$ $(j = p, v)$ are controller parameters to be designed.

Remark 3. *Compared with directly employing the binary-form characteristic indices in (13) and (14), the hierarchical coupling/disturbance adaptive utilization mechanisms developed in this paper offer the following two advantages: (1) the chattering phenomenon induced by the switching of the characteristic indices is effectively avoided, resulting in smoother utilization or compensation of coupling/disturbances; (2) the proposed mechanisms not only exploit beneficial coupling/disturbances but also utilize the negative of detrimental ones. Taking $J_{v,i}$ as an illustrative example, as shown in Figure 3, when $J_{v,i} < 0$ (red region), a portion of the beneficial disturbance is utilized; when $J_{v,i} \geq 0$ (blue region), the detrimental disturbance is not only fully compensated but also partially exploited in a reverse manner.*

Remark 4. *It should be noted that Equation (16) is formulated in terms of $\hat{\boldsymbol{d}}_v$ rather than $\boldsymbol{d}_v$, because $\boldsymbol{d}_v$ is not directly available in practical systems. Accordingly, employing $\hat{\boldsymbol{d}}_v$ serves as an implementable surrogate and preserves closed-loop stability, as established in Section 3.3. To reduce the impact of the disturbance estimation error $\tilde{\boldsymbol{d}}_v$ on the proposed C/D-AUM, we adopt a finite-time convergent ST-SMO to estimate $\boldsymbol{d}_v$, thereby expediting the convergence of the estimate. Moreover, a sign mismatch between $\hat{\boldsymbol{d}}_v$ and $\boldsymbol{d}_v$ is prone to occur when $\boldsymbol{d}_v$ lies in a small neighborhood of the origin or when $\boldsymbol{d}_v$ changes sign. As reported in [30], this issue does not degrade the performance of the disturbance-utilization control framework. A related practical remedy is the threshold-based*

compensation activation mechanism proposed in [31], which enables disturbance compensation only when the estimation error is below a prescribed bound.

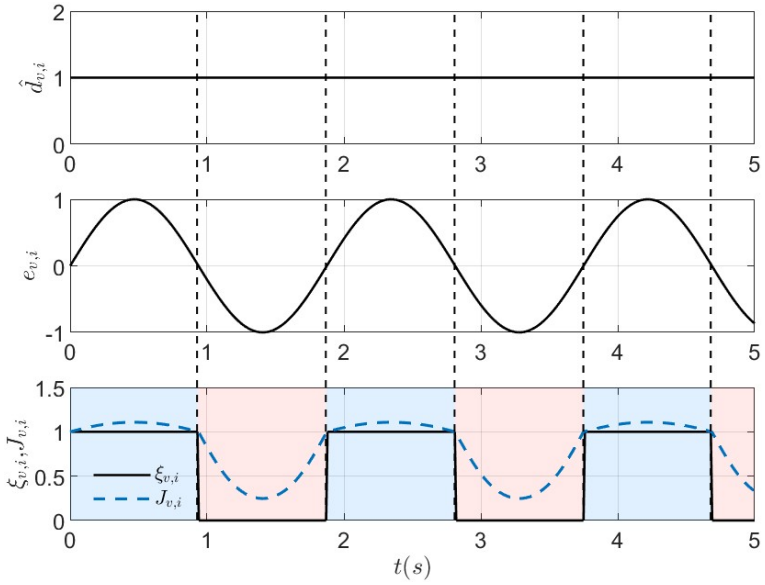


Figure 3. Illustration of the coupling/disturbance adaptive utilization mechanisms.

3.1.3. RTC Law Design

To achieve rapid convergence of position tracking errors, the robust tracking control law for the position loop is designed by incorporating the C/D-AUM in (15) as:

$$\boldsymbol{v}_d = -\boldsymbol{k}_{p,1}\,\mathrm{sig}^{\gamma_{p,1}}(\boldsymbol{e}_p) - \boldsymbol{k}_{p,2}\,\mathrm{sig}^{\gamma_{p,2}}(\boldsymbol{e}_p) + \dot{\boldsymbol{p}}_c - \boldsymbol{\xi}_p \otimes \boldsymbol{e}_v, \tag{17}$$

where $\boldsymbol{k}_{p,1} = \mathrm{diag}\{k_{p,11}, k_{p,12}, k_{p,13}\}$, $\boldsymbol{k}_{p,2} = \mathrm{diag}\{k_{p,21}, k_{p,22}, k_{p,23}\}$, $\gamma_{p,1} \geq 1$, and $0 < \gamma_{p,2} < 1$ are positive design parameters, and $\otimes$ denotes the element-wise multiplication (Hadamard product).

In the velocity loop, by incorporating the lumped-disturbance estimate in (11) and the C/D-AUM in (16), the robust tracking control law is designed as:

$$\boldsymbol{f}_{a,c} = \boldsymbol{G}_v^{-1}\left(-\boldsymbol{k}_{v,1}\,\mathrm{sig}^{\gamma_{v,1}}(\boldsymbol{e}_v) - \boldsymbol{k}_{v,2}\,\mathrm{sig}^{\gamma_{v,2}}(\boldsymbol{e}_v) - \boldsymbol{f}_v + \dot{\boldsymbol{v}}_c - \boldsymbol{\xi}_v \otimes \hat{\boldsymbol{d}}_v\right), \tag{18}$$

where $\boldsymbol{k}_{v,1} = \mathrm{diag}\{k_{v,11}, k_{v,12}, k_{v,13}\}$, $\boldsymbol{k}_{v,2} = \mathrm{diag}\{k_{v,21}, k_{v,22}, k_{v,23}\}$, $\gamma_{v,1} \geq 1$, and $0 < \gamma_{v,2} < 1$ are positive design parameters. Moreover, $\dot{\boldsymbol{v}}_c$ is generated by the first-order filter $t_v\dot{\boldsymbol{v}}_c + \boldsymbol{v}_c = \boldsymbol{v}_d$.

3.2. Rotational Control Subsystem

3.2.1. ST-SMO Design

Similar to (11), the ST-SMO for the attitude dynamics (2) is constructed as:

$$\begin{cases} \dot{\hat{\boldsymbol{\omega}}} = \boldsymbol{G}_\omega \boldsymbol{\tau}_a + \boldsymbol{f}_\omega - L_\omega^{1/2}\boldsymbol{\lambda}_{\omega,1}\mathbf{sig}^{1/2}(\hat{\boldsymbol{\omega}} - \boldsymbol{\omega}) + \hat{\boldsymbol{d}}_\omega, \\ \dot{\hat{\boldsymbol{d}}}_\omega = -L_\omega\boldsymbol{\lambda}_{\omega,2}\mathbf{sgn}(\hat{\boldsymbol{\omega}} - \boldsymbol{\omega}), \end{cases} \tag{19}$$

where $\hat{\boldsymbol{\omega}}$ and $\hat{\boldsymbol{d}}_\omega$ denote the estimates of $\boldsymbol{\omega}$ and $\boldsymbol{d}_\omega$, respectively; $\boldsymbol{\lambda}_{\omega,1} = \mathrm{diag}\{\lambda_{\omega,11}, \lambda_{\omega,12}, \lambda_{\omega,13}\}$ and $\boldsymbol{\lambda}_{\omega,2} = \mathrm{diag}\{\lambda_{\omega,21}, \lambda_{\omega,22}, \lambda_{\omega,23}\}$ are positive observer gain matrices. The state estimation error $\tilde{\boldsymbol{\omega}} = \hat{\boldsymbol{\omega}} - \boldsymbol{\omega}$ and the disturbance estimation error $\tilde{\boldsymbol{d}}_\omega = \hat{\boldsymbol{d}}_\omega - \boldsymbol{d}_\omega$ exhibit finite-time convergence. The corresponding analysis is provided in Section 3.1.1.

3.2.2. C/D-AUM Design

In the rotational control subsystem, the coupling characteristic indices $\boldsymbol{J}_\Omega = [J_{\Omega,1}, J_{\Omega,2}, J_{\Omega,3}]^{\mathrm{T}}$ and the disturbance characteristic indices $\boldsymbol{J}_\omega = [J_{\omega,1}, J_{\omega,2}, J_{\omega,3}]^{\mathrm{T}}$ are defined as:

$$J_{\Omega,i} = \begin{cases} 1, & \mathrm{sgn}(e_{\Omega,i} e_{\omega,i}) \geq 0, \\ 0, & \mathrm{sgn}(e_{\Omega,i} e_{\omega,i}) < 0, \end{cases} \tag{20}$$

$$J_{\omega,i} = \begin{cases} 1, & \mathrm{sgn}(e_{\omega,i} \hat{d}_{\omega,i}) \geq 0, \\ 0, & \mathrm{sgn}(e_{\omega,i} \hat{d}_{\omega,i}) < 0, \end{cases} \tag{21}$$

where $i = 1, 2, 3$ denotes the three channels of the rotational dynamics. The interpretations of the coupling characteristic indices and the disturbance indices are the same as those in (13) and (14) and are therefore omitted for brevity.

Based on (20) and (21), the hierarchical coupling/disturbance adaptive utilization mechanisms $\boldsymbol{\xi}_\Omega = [\xi_{\Omega,1}, \xi_{\Omega,2}, \xi_{\Omega,3}]^{\mathrm{T}}$ and $\boldsymbol{\xi}_\omega = [\xi_{\omega,1}, \xi_{\omega,2}, \xi_{\omega,3}]^{\mathrm{T}}$ are designed as:

$$\xi_{\Omega,i} = c_{\Omega,1i} \tanh(\eta_{\Omega,i} |e_{\Omega,i}|) \,\mathrm{sgn}(e_{\Omega,i} e_{\omega,i}) + \left(1 - c_{\Omega,2i} \tanh(\eta_{\Omega,i} |e_{\Omega,i}|)\right), \tag{22}$$

$$\xi_{\omega,i} = c_{\omega,1i} \tanh(\eta_{\omega,i} |e_{\omega,i}|) \,\mathrm{sgn}(e_{\omega,i} \hat{d}_{\omega,i}) + \left(1 - c_{\omega,2i} \tanh(\eta_{\omega,i} |e_{\omega,i}|)\right), \tag{23}$$

where $c_{j,1i} > c_{j,2i} > 0$, and $\eta_{j,i} > 0$ $(j = \Omega, \omega)$ are controller parameters to be designed.

3.2.3. RTC Law Design

By incorporating the C/D-AUM in (20), the robust tracking control law for the attitude angle loop is designed as:

$$\boldsymbol{\omega}_d = \bar{\boldsymbol{G}}_\Omega^{-1} \left(-\boldsymbol{k}_{\Omega,1} \,\mathrm{sig}^{\gamma_{\Omega,1}}(\boldsymbol{e}_\Omega) - \boldsymbol{k}_{\Omega,2} \,\mathrm{sig}^{\gamma_{\Omega,2}}(\boldsymbol{e}_\Omega) - \boldsymbol{f}_\Omega + \dot{\boldsymbol{\Omega}}_c - \bar{\boldsymbol{G}}_\Omega (\boldsymbol{\xi}_\Omega \otimes \boldsymbol{e}_\omega)\right), \tag{24}$$

where $\boldsymbol{k}_{\Omega,1} = \mathrm{diag}\{k_{\Omega,11}, k_{\Omega,12}, k_{\Omega,13}\}$, $\boldsymbol{k}_{\Omega,2} = \mathrm{diag}\{k_{\Omega,21}, k_{\Omega,22}, k_{\Omega,23}\}$, $\gamma_{\Omega,1} \geq 1$, and $0 < \gamma_{\Omega,2} < 1$ are positive design parameters.

In the angular rate loop, by incorporating the lumped-disturbance estimate in (19) and the C/D-AUM in (21), the robust tracking control law is designed as:

$$\boldsymbol{\tau}_{a,c} = \boldsymbol{G}_\omega^{-1} \left(-\boldsymbol{k}_{\omega,1} \,\mathrm{sig}^{\gamma_{\omega,1}}(\boldsymbol{e}_\omega) - \boldsymbol{k}_{\omega,2} \,\mathrm{sig}^{\gamma_{\omega,2}}(\boldsymbol{e}_\omega) - \boldsymbol{f}_\omega + \dot{\boldsymbol{\omega}}_c - \boldsymbol{\xi}_\omega \otimes \hat{\boldsymbol{d}}_\omega\right), \tag{25}$$

where $\boldsymbol{k}_{\omega,1} = \mathrm{diag}\{k_{\omega,11}, k_{\omega,12}, k_{\omega,13}\}$, $\boldsymbol{k}_{\omega,2} = \mathrm{diag}\{k_{\omega,21}, k_{\omega,22}, k_{\omega,23}\}$, $\gamma_{\omega,1} \geq 1$, and $0 < \gamma_{\omega,2} < 1$ are positive design parameters. Moreover, $\dot{\boldsymbol{\omega}}_c$ is generated by the first-order filter $t_\omega \dot{\boldsymbol{\omega}}_c + \boldsymbol{\omega}_c = \boldsymbol{\omega}_d$.

3.2.4. Control Allocation and Inverse Mapping

After obtaining the desired force in (18) and the desired torque in (25), the virtual control input $\boldsymbol{N}$ can be given by:

$$\boldsymbol{N} = \boldsymbol{A}^{\dagger} \begin{bmatrix} \boldsymbol{f}_{a,c} \\ \boldsymbol{\tau}_{a,c} \end{bmatrix}, \tag{26}$$

where $\boldsymbol{A}^{\dagger}$ denotes the Moore–Penrose pseudo-inverse of $\boldsymbol{A}$.

Due to the inability of pseudo-inverse control allocation to account for actuator saturation issues, the geometric saturation model proposed in [24] is further applied to modify $\boldsymbol{N}$, resulting in $\boldsymbol{N}_s$, which satisfies the actuator saturation constraints. Finally, according to Equation (8), the actual control inputs are obtained as follows:

$$\begin{cases} \alpha_i = \arctan\left(\dfrac{N_{s,l,i}}{N_{s,v,i}}\right), \\ n_i = \sqrt{\dfrac{N_{s,l,i}^2 + N_{s,v,i}^2}{c_T}}. \end{cases} \tag{27}$$

3.3. Stability Analysis

This section analyzes the stability of the closed-loop system and elucidates the role of the proposed hierarchical adaptive coupling/disturbance utilization mechanisms.

Theorem 1. *Consider the tiltable quadrotor system described by (1) and (2). Under the control laws (17), (18), (24), and (25), together with the ST-SMOs (11) and (19) and the C/D-AUMs (13), (14), (20), and (21), all the closed-loop error states are uniformly ultimately bounded.*

Proof. Consider the following Lyapunov function candidate:

$$V = \frac{1}{2}\boldsymbol{e}_p^{\mathrm{T}}\boldsymbol{e}_p + \frac{1}{2}\boldsymbol{e}_v^{\mathrm{T}}\boldsymbol{e}_v + \frac{1}{2}\boldsymbol{e}_\Omega^{\mathrm{T}}\boldsymbol{e}_\Omega + \frac{1}{2}\boldsymbol{e}_\omega^{\mathrm{T}}\boldsymbol{e}_\omega + \frac{1}{2}\bar{\boldsymbol{e}}_v^{\mathrm{T}}\bar{\boldsymbol{e}}_v + \frac{1}{2}\bar{\boldsymbol{e}}_\omega^{\mathrm{T}}\bar{\boldsymbol{e}}_\omega, \tag{28}$$

where $\bar{\boldsymbol{e}}_v = \boldsymbol{v}_c - \boldsymbol{v}_d$ and $\bar{\boldsymbol{e}}_\omega = \boldsymbol{\omega}_c - \boldsymbol{\omega}_d$ denote the filter errors.

Taking the time derivative of V yields:

$$\dot{V} = \boldsymbol{e}_p^{\mathrm{T}}\dot{\boldsymbol{e}}_p + \boldsymbol{e}_v^{\mathrm{T}}\dot{\boldsymbol{e}}_v + \boldsymbol{e}_\Omega^{\mathrm{T}}\dot{\boldsymbol{e}}_\Omega + \boldsymbol{e}_\omega^{\mathrm{T}}\dot{\boldsymbol{e}}_\omega + \bar{\boldsymbol{e}}_v^{\mathrm{T}}\dot{\bar{\boldsymbol{e}}}_v + \bar{\boldsymbol{e}}_\omega^{\mathrm{T}}\dot{\bar{\boldsymbol{e}}}_\omega. \tag{29}$$

Recalling the filter definitions in (18) and (25), the following error dynamics are obtained:

$$\dot{\bar{\boldsymbol{e}}}_v = -\frac{\bar{\boldsymbol{e}}_v}{t_v} - \dot{\boldsymbol{v}}_d, \dot{\bar{\boldsymbol{e}}}_\omega = -\frac{\bar{\boldsymbol{e}}_\omega}{t_\omega} - \dot{\boldsymbol{\omega}}_d. \tag{30}$$

Substituting the control laws (17), (18), (24), and (25), together with the ST-SMOs (11) and (19) and the C/D-AUMs (13), (14), (20), and (21) into the error dynamics (9) and (10), and further into (29), yields:

$$\begin{aligned} \dot{V} = {} & \boldsymbol{e}_p^{\mathrm{T}}\left(\boldsymbol{e}_v + \bar{\boldsymbol{e}}_v - \boldsymbol{k}_{p,1}\,\mathrm{sig}^{\gamma_{p,1}}(\boldsymbol{e}_p) - \boldsymbol{k}_{p,2}\,\mathrm{sig}^{\gamma_{p,2}}(\boldsymbol{e}_p) - \boldsymbol{\xi}_p \otimes \boldsymbol{e}_v\right) \\ & + \boldsymbol{e}_v^{\mathrm{T}}\left(-\boldsymbol{k}_{v,1}\,\mathrm{sig}^{\gamma_{v,1}}(\boldsymbol{e}_v) - \boldsymbol{k}_{v,2}\,\mathrm{sig}^{\gamma_{v,2}}(\boldsymbol{e}_v) - \boldsymbol{\xi}_v \otimes \hat{\boldsymbol{d}}_v + \boldsymbol{d}_v\right) \\ & + \boldsymbol{e}_\Omega^{\mathrm{T}}\left(\bar{\boldsymbol{G}}_\Omega\boldsymbol{e}_\omega - \boldsymbol{k}_{\Omega,1}\,\mathrm{sig}^{\gamma_{\Omega,1}}(\boldsymbol{e}_\Omega) - \boldsymbol{k}_{\Omega,2}\,\mathrm{sig}^{\gamma_{\Omega,2}}(\boldsymbol{e}_\Omega) - \bar{\boldsymbol{G}}_\Omega(\boldsymbol{\xi}_\Omega \otimes \boldsymbol{e}_\omega) + \bar{\boldsymbol{G}}_\Omega\bar{\boldsymbol{e}}_\omega\right) \\ & + \boldsymbol{e}_\omega^{\mathrm{T}}\left(-\boldsymbol{k}_{\omega,1}\,\mathrm{sig}^{\gamma_{\omega,1}}(\boldsymbol{e}_\omega) - \boldsymbol{k}_{\omega,2}\,\mathrm{sig}^{\gamma_{\omega,2}}(\boldsymbol{e}_\omega) - \boldsymbol{\xi}_\omega \otimes \hat{\boldsymbol{d}}_\omega + \boldsymbol{d}_\omega\right) \\ & + \bar{\boldsymbol{e}}_v^{\mathrm{T}}\left(-\frac{\bar{\boldsymbol{e}}_v}{t_v} - \dot{\boldsymbol{v}}_d\right) + \bar{\boldsymbol{e}}_\omega^{\mathrm{T}}\left(-\frac{\bar{\boldsymbol{e}}_\omega}{t_\omega} - \dot{\boldsymbol{\omega}}_d\right). \end{aligned} \tag{31}$$

Next, consider the coupling/disturbance adaptive utilization terms $\boldsymbol{e}_p^{\mathrm{T}}(\boldsymbol{e}_v - \boldsymbol{\xi}_p \otimes \boldsymbol{e}_v)$, $\boldsymbol{e}_\Omega^{\mathrm{T}}(\bar{\boldsymbol{G}}_\Omega\boldsymbol{e}_\omega - \bar{\boldsymbol{G}}_\Omega(\boldsymbol{\xi}_\Omega \otimes \boldsymbol{e}_\omega))$, $\boldsymbol{e}_v^{\mathrm{T}}(-\boldsymbol{\xi}_v \otimes \hat{\boldsymbol{d}}_v + \boldsymbol{d}_v)$, and $\boldsymbol{e}_\omega^{\mathrm{T}}(-\boldsymbol{\xi}_\omega \otimes \hat{\boldsymbol{d}}_\omega + \boldsymbol{d}_\omega)$. To illustrate the analysis, the terms $\boldsymbol{e}_p^{\mathrm{T}}(\boldsymbol{e}_v - \boldsymbol{\xi}_p \otimes \boldsymbol{e}_v)$ and $\boldsymbol{e}_v^{\mathrm{T}}(-\boldsymbol{\xi}_v \otimes \hat{\boldsymbol{d}}_v + \boldsymbol{d}_v)$ are selected as representative examples. Noting that $\boldsymbol{\xi}_p \otimes \boldsymbol{e}_v = [\xi_{p,1}e_{v,1}, \xi_{p,2}e_{v,2}, \xi_{p,3}e_{v,3}]^{\mathrm{T}}$, $0 \le \tanh(\eta_{p,i}|e_{p,i}|) < 1$, and $|e_{p,i}e_{v,i}| - e_{p,i}e_{v,i} \ge 0$, and assuming that $c_{p,1i} > c_{p,2i} > 0$ and $c_{v,1i} > c_{v,2i} > 0$, the following inequalities hold:

$$\begin{aligned}
\boldsymbol{e}_p^{\mathrm{T}}(\boldsymbol{e}_v - \boldsymbol{\xi}_p \otimes \boldsymbol{e}_v) &= \sum_{i=1}^{3}(1-\xi_{p,i})\, e_{p,i}\, e_{v,i} \\
&= \sum_{i=1}^{3}\Big(-c_{p,1i}\tanh(\eta_{p,i}|e_{p,i}|)\,\mathrm{sgn}(e_{p,i}e_{v,i})\, e_{p,i}\, e_{v,i} + c_{p,2i}\tanh(\eta_{p,i}|e_{p,i}|)\, e_{p,i}\, e_{v,i}\Big) \\
&= \sum_{i=1}^{3}\Big(-c_{p,1i}\tanh(\eta_{p,i}|e_{p,i}|)\,|e_{p,i}e_{v,i}| + c_{p,2i}\tanh(\eta_{p,i}|e_{p,i}|)\, e_{p,i}\, e_{v,i}\Big) \\
&\le \sum_{i=1}^{3} -c_{p,2i}\tanh(\eta_{p,i}|e_{p,i}|)\big(|e_{p,i}e_{v,i}| - e_{p,i}e_{v,i}\big) \le 0.
\end{aligned} \tag{32}$$

$$\begin{aligned}
\boldsymbol{e}_v^{\mathrm{T}}(-\boldsymbol{\xi}_v \otimes \hat{\boldsymbol{d}}_v + \boldsymbol{d}_v) &= \sum_{i=1}^{3}\Big(-c_{v,1i}\tanh(\eta_{v,i}|e_{v,i}|)\,\mathrm{sgn}(e_{v,i}\hat{d}_{v,i})e_{v,i}\hat{d}_{v,i} - \big(1 - c_{v,2i}\tanh(\eta_{v,i}|e_{v,i}|)\big)e_{v,i}\hat{d}_{v,i} + e_{v,i}d_{v,i}\Big) \\
&\le \sum_{i=1}^{3}\Big(-c_{v,2i}\tanh(\eta_{v,i}|e_{v,i}|)\big(|e_{v,i}\hat{d}_{v,i}| - e_{v,i}\hat{d}_{v,i}\big) - e_{v,i}\tilde{d}_{v,i}\Big) \\
&\le \sum_{i=1}^{3} -e_{v,i}\tilde{d}_{v,i} = -\boldsymbol{e}_v^{\mathrm{T}}\tilde{\boldsymbol{d}}_v,
\end{aligned} \tag{33}$$

where $\tilde{\boldsymbol{d}}_v$ denotes the disturbance estimation error.

Then, the error-related terms are further analyzed. Consider $\boldsymbol{e}_p^{\mathrm{T}}\big(-\boldsymbol{k}_{p,1}\,\mathrm{sig}^{\gamma_{p,1}}(\boldsymbol{e}_p) - \boldsymbol{k}_{p,2}\,\mathrm{sig}^{\gamma_{p,2}}(\boldsymbol{e}_p)\big)$. Since $\gamma_{p,1} \ge 1$ and $0 < \gamma_{p,2} < 1$, for any $x \in \mathbb{R}$, it holds that $|x|^{\gamma_{p,1}+1} \ge |x|^2$ when $|x| \ge 1$, and $|x|^{\gamma_{p,2}+1} \ge |x|^2$ when $|x| \le 1$. Therefore,

$$\begin{aligned}
\boldsymbol{e}_p^{\mathrm{T}}\big(-\boldsymbol{k}_{p,1}\,\mathrm{sig}^{\gamma_{p,1}}(\boldsymbol{e}_p) - \boldsymbol{k}_{p,2}\,\mathrm{sig}^{\gamma_{p,2}}(\boldsymbol{e}_p)\big) &= -\sum_{i=1}^{3}\Big(k_{p,1i}\,|e_{p,i}|^{\gamma_{p,1}+1} + k_{p,2i}\,|e_{p,i}|^{\gamma_{p,2}+1}\Big) \\
&\le -\sum_{i=1}^{3}\Big(k_{p,1i}\,|e_{p,i}|^{2} + k_{p,2i}\,|e_{p,i}|^{2}\Big) \\
&\le -k_p\,\boldsymbol{e}_p^{\mathrm{T}}\boldsymbol{e}_p,
\end{aligned} \tag{34}$$

where $k_p = \min\big\{\lambda_{\min}(\boldsymbol{k}_{p,1}), \lambda_{\min}(\boldsymbol{k}_{p,2})\big\} > 0$.

Substituting (32), (33), and (34) into (31) and invoking Young's inequality yield:

$$\begin{aligned}
\dot{V} =\ & \boldsymbol{e}_p^{\mathrm{T}}\bar{\boldsymbol{e}}_v - k_p\boldsymbol{e}_p^{\mathrm{T}}\boldsymbol{e}_p - k_v\boldsymbol{e}_v^{\mathrm{T}}\boldsymbol{e}_v - \boldsymbol{e}_v^{\mathrm{T}}\tilde{\boldsymbol{d}}_v - k_\Omega\boldsymbol{e}_\Omega^{\mathrm{T}}\boldsymbol{e}_\Omega + \boldsymbol{e}_\Omega^{\mathrm{T}}\bar{\boldsymbol{G}}_\Omega\bar{\boldsymbol{e}}_\omega \\
& - k_\omega\boldsymbol{e}_\omega^{\mathrm{T}}\boldsymbol{e}_\omega - \boldsymbol{e}_\omega^{\mathrm{T}}\tilde{\boldsymbol{d}}_\omega - \frac{1}{t_v}\bar{\boldsymbol{e}}_v^{\mathrm{T}}\bar{\boldsymbol{e}}_v - \bar{\boldsymbol{e}}_v^{\mathrm{T}}\dot{\boldsymbol{v}}_d - \frac{1}{t_\omega}\bar{\boldsymbol{e}}_\omega^{\mathrm{T}}\bar{\boldsymbol{e}}_\omega - \bar{\boldsymbol{e}}_\omega^{\mathrm{T}}\dot{\boldsymbol{\omega}}_d \\
\le\ & -\Big(k_p - \frac{1}{2}\Big)\boldsymbol{e}_p^{\mathrm{T}}\boldsymbol{e}_p - \Big(k_v - \frac{1}{2}\Big)\boldsymbol{e}_v^{\mathrm{T}}\boldsymbol{e}_v - \Big(k_\Omega - \frac{\|\bar{\boldsymbol{G}}_\Omega\|}{2}\Big)\boldsymbol{e}_\Omega^{\mathrm{T}}\boldsymbol{e}_\Omega - \Big(k_\omega - \frac{1}{2}\Big)\boldsymbol{e}_\omega^{\mathrm{T}}\boldsymbol{e}_\omega \\
& - \Big(\frac{1}{t_v} - 1\Big)\bar{\boldsymbol{e}}_v^{\mathrm{T}}\bar{\boldsymbol{e}}_v - \Big(\frac{1}{t_\omega} - 1\Big)\bar{\boldsymbol{e}}_\omega^{\mathrm{T}}\bar{\boldsymbol{e}}_\omega + \frac{1}{2}\bar{d}_v^2 + \frac{1}{2}\bar{d}_\omega^2 + \frac{1}{2}\sigma_v^2 + \frac{1}{2}\sigma_\omega^2 \\
\le\ & -2cV + \Delta,
\end{aligned} \tag{35}$$

where $c = \min\Big\{k_p - \frac{1}{2},\ k_v - \frac{1}{2},\ k_\Omega - \frac{\|\bar{G}_\Omega\|}{2},\ k_\omega - \frac{1}{2},\ \frac{1}{t_v} - 1,\ \frac{1}{t_\omega} - 1\Big\}$, $\Delta = \frac{1}{2}\bar{d}_v^2 + \frac{1}{2}\bar{d}_\omega^2 + \frac{1}{2}\sigma_v^2 + \frac{1}{2}\sigma_\omega^2$. Here, $\bar{d}_v$, $\bar{d}_\omega$, σ_v, and σ_ω are positive constants satisfying $\|\tilde{\boldsymbol{d}}_v\| \le \bar{d}_v$, $\|\tilde{\boldsymbol{d}}_\omega\| \le \bar{d}_\omega$, $\|\dot{\boldsymbol{v}}_d\| \le \sigma_v$, and $\|\dot{\boldsymbol{\omega}}_d\| \le \sigma_\omega$. This completes the proof. □

The effect of the proposed hierarchical coupling/disturbance adaptive utilization mechanisms can be further elucidated through Lyapunov stability analysis. Specifically, consider the term $L_{p,i} = e_{p,i}^{\mathrm{T}}\big(e_{v,i} - \xi_{p,i}e_{v,i}\big)$. Based on (32), $L_{p,i}$ can be reformulated as:

$$L_{p,i} = \big[-c_{p,1i}\,\mathrm{sgn}(e_{p,i}e_{v,i}) + c_{p,2i}\big]\tanh(\eta_{p,i}|e_{p,i}|)\, e_{p,i}e_{v,i}. \tag{36}$$

When $\mathrm{sgn}(e_{p,i}e_{v,i}) > 0$, it follows that

$$L_{p,i} = \left(-c_{p,1i} + c_{p,2i}\right) \tanh\left(\eta_{p,i}|e_{p,i}|\right) e_{p,i}e_{v,i} < 0, \tag{37}$$

which indicates that $L_{p,i}$ is consistent with the sign of $\dot{V}$ and therefore contributes to accelerating the convergence of the Lyapunov function V.

Furthermore, considering the limiting cases, one has

$$\lim_{|e_{p,i}|\to 0} \left(-c_{p,1i} + c_{p,2i}\right) \tanh\left(\eta_{p,i}|e_{p,i}|\right) e_{v,i} = 0, \tag{38}$$

$$\lim_{|e_{p,i}|\to \infty} \left(-c_{p,1i} + c_{p,2i}\right) \tanh\left(\eta_{p,i}|e_{p,i}|\right) e_{v,i} = \left(-c_{p,1i} + c_{p,2i}\right) e_{v,i}. \tag{39}$$

These results demonstrate that the proposed hierarchical coupling/disturbance adaptive utilization mechanisms enable a smooth and bounded utilization of coupling and disturbance effects. Moreover, the proposed mechanisms not only effectively exploit beneficial coupling/disturbances but also partially exploit detrimental coupling/disturbances in a reverse manner.

Remark 5. *To facilitate practical implementation, a brief guideline for tuning the parameters of the proposed controller is provided. First, for the controller parameters, the exponents in the error power terms are typically selected as* $\gamma_{i,1} = 1.2$ *and* $\gamma_{i,2} = 0.8 (i \in \{p, v, \Omega, \omega\})$. *The control gains* $k_{i,1j} > 0$ $(i \in \{p, v, \Omega, \omega\},\ j = 1, 2, 3)$ *should be chosen positive and generally follow the rule that the inner loop gains are larger than the outer loop gains. Second, for the observer parameters,* $\lambda_{i,1j}$ *and* $\lambda_{i,2j} (i \in \{v, \omega\}, j = 1, 2, 3)$ *can be set to* 1.5 *and* 1.1, *respectively. The gain* $L_i (i \in \{v, \omega\})$ *is related to the differential upper bound of the lumped disturbance and should be selected larger than this bound. Finally, for the C/D-AUM parameters,* $\eta_{j,i} > 0$ $(j \in \{p, v, \Omega, \omega\},\ i = 1, 2, 3)$ *can be interpreted as a smoothing factor. If* $\eta_{j,i}$ *is too large,* $\tanh(\cdot)$ *tends to behave like the sign function, which may induce chattering. The parameters* $c_{j,1i}$ *and* $c_{j,2i} (j \in \{p, v, \Omega, \omega\},\ i = 1, 2, 3)$ *should satisfy* $c_{j,1i} > c_{j,2i} > 0$. *When the disturbance/coupling is beneficial,* $(c_{j,1i} + c_{j,2i})$ *represents the maximum utilization factor of the disturbance/coupling. When it is detrimental,* $-(c_{j,1i} - c_{j,2i})$ *represents the maximum utilization factor of the disturbance/coupling.*

4. Simulation Results

In this section, comparative simulations and Monte Carlo simulations are conducted to verify the effectiveness and robustness of the proposed hierarchical adaptive coupling/disturbance utilization control method.

4.1. Comparative Simulations

In the simulations, the physical and geometric parameters of the tiltable quadrotor are adopted from [24], while the dynamic parameters are estimated using the parameter estimation platform (https://www.flyeval.cn/ (accessed on on 25 April 2025)). Based on the dynamic analysis and control capability constraints, the control inputs are limited to $0 < n_i < 800$ rad/s and $-60^\circ < \alpha_i < 60^\circ$ to ensure flight safety.

Two control methods are employed for comparison: (1) the Flexible Disturbance Compensation Control (FDCC) method [24], and (2) the proposed control scheme without the coupling/disturbance adaptive utilization mechanism (denoted as "Proposed w/o C/D-AUM"). These comparisons are conducted to validate the effectiveness of the proposed control framework as well as the hierarchical coupling/disturbance adaptive utilization mechanism.

The simulation scenario is configured as follows. The tiltable quadrotor first takes off to an altitude of 5 m and then tracks a square reference trajectory with a side length of

5 m in the horizontal plane. To evaluate the control capability when position and attitude maneuvers are performed simultaneously, the attitude angle commands are varied within $[-15^\circ, 15^\circ]$ during the position maneuver. The control parameters used in the simulations are summarized in Table 1. The model uncertainties are introduced as $+20\%$ variations, such that $\Delta G_v = 0.2G_v, \Delta f_v = 0.2f_v, \Delta G_\omega = 0.2G_\omega, \Delta f_\omega = 0.2f_\omega$. The external disturbances are given by

$$\mathbf{d}_{v,\mathrm{ex}} = k_{d_v} \begin{bmatrix} 0.8\sin(0.3t) \\ 0.6\sin(0.2t) \\ 0.7\sin(0.3t) \end{bmatrix}, \quad \mathbf{d}_{\omega,\mathrm{ex}} = k_{d_\omega} \begin{bmatrix} 1.4\sin(0.2t) \\ 1.5\sin(0.3t) \\ 1.6\sin(0.2t) \end{bmatrix}. \tag{40}$$

where $k_{d_v} = k_{d_\omega} = 1$.

Table 1. Controller parameters.

Method	Parameter
FDCC	$\eta_v = \eta_\omega = 0.08$, $\omega_{n,p} = \omega_{n,\Omega} = 0.8$, $\zeta_p = \zeta_\Omega = 20$, $c_{p,1} = c_{\Omega,1} = 8$, $c_{p,2} = c_{\Omega,2} = 16$, $k_p = 1$, $k_v = 3$, $k_\Omega = 3$, $k_\omega = 5$. $\lambda_{v,1} = \lambda_{\omega,1} = \mathrm{diag}\{1.5, 1.5, 1.5\}$, $\lambda_{v,2} = \lambda_{\omega,2} = \mathrm{diag}\{1.1, 1.1, 1.1\}$, $L_v = L_\omega = 0.8$, $\gamma_{p,1} = \gamma_{v,1} = \gamma_{\Omega,1} = \gamma_{\omega,1} = 1.2$, $\gamma_{p,2} = \gamma_{v,2} = \gamma_{\Omega,2} = \gamma_{\omega,2} = 0.8$, $\boldsymbol{c}_{p,1} = \mathrm{diag}\{0.3, 0.3, 0.3\}$, $\boldsymbol{c}_{p,2} = \mathrm{diag}\{0.1, 0.1, 0.1\}$, $\boldsymbol{\eta}_p = \mathrm{diag}\{1, 1, 1\}$, $\boldsymbol{c}_{v,1} = \mathrm{diag}\{0.5, 0.5, 0.5\}$, $\boldsymbol{c}_{v,2} = \mathrm{diag}\{0.3, 0.3, 0.3\}$, $\boldsymbol{\eta}_v = \mathrm{diag}\{1, 1, 1\}$, $\boldsymbol{k}_{p,1} = \mathrm{diag}\{1, 1, 1\}$, $\boldsymbol{k}_{p,2} = \mathrm{diag}\{1, 1, 1\}$, $\boldsymbol{k}_{v,1} = \mathrm{diag}\{1.5, 1.5, 1.5\}$, $\boldsymbol{k}_{v,2} = \mathrm{diag}\{1.5, 1.5, 5\}$, $\boldsymbol{c}_{\Omega,1} = \mathrm{diag}\{2, 2, 2\}$, $\boldsymbol{c}_{\Omega,2} = \mathrm{diag}\{0.5, 0.5, 0.5\}$, $\boldsymbol{\eta}_\Omega = \mathrm{diag}\{1, 1, 1\}$, $\boldsymbol{c}_{\omega,1} = \mathrm{diag}\{1.8, 1.8, 1.8\}$, $\boldsymbol{c}_{\omega,2} = \mathrm{diag}\{0.5, 0.5, 0.5\}$, $\boldsymbol{\eta}_\omega = \mathrm{diag}\{1, 1, 1\}$, $\boldsymbol{k}_{\Omega,1} = \mathrm{diag}\{3, 3, 3\}$, $\boldsymbol{k}_{\Omega,2} = \mathrm{diag}\{3, 3, 3\}$, $\boldsymbol{k}_{\omega,1} = \mathrm{diag}\{5, 5, 5\}$, $\boldsymbol{k}_{\omega,2} = \mathrm{diag}\{5, 5, 5\}$.
Proposed method, Proposed w/o C/D-AUM	

Figure 4 shows the position and velocity tracking curves (with the z-axis of the inertial coordinate system pointing downward, using altitude to replace the z-coordinate). It can be observed that both the proposed method and the comparison methods achieve good tracking control accuracy. Since the desired velocity commands for the proposed and comparison methods differ, to avoid redundancy, only the velocity tracking curves for the proposed method are shown in Figure 4c.

To better highlight the comparison between the proposed method and the comparison methods, Figures 5 and 6 show the three-axis position/velocity errors and the three-axis C/D-AUM outputs. From the zoomed-in view (blue dashed line) in Figure 5a–c, it can be observed that the proposed hierarchical C/D-AUM significantly improves the position-loop tracking accuracy by effectively exploiting the velocity tracking error as a coupling state. As shown in Figure 6a–c, since both the proposed method and the FDCC employ a disturbance utilization mechanism in the inner loop, they achieve better tracking performance than the Proposed w/o C/D-AUM scheme. Additionally, by combining Figures 5 and 6, it is confirmed that using disturbances only in the inner loop (velocity, angular rate) does not improve the tracking performance of the outer loop (position, angle), thus validating the effectiveness of the proposed hierarchical C/D-AUM.

Figure 7 presents the performance curves of the rotational control subsystem (attitude angles and angular rates). Similarly, to avoid redundancy, only the angular rate tracking curves for the proposed method are shown in Figure 7b. Figures 8 and 9 show the three-axis angle/angular rate tracking errors and the corresponding three-axis C/D-AUM output

curves. It can be observed that, under the proposed method, the tracking performance of both the outer loop (attitude) and the inner loop (angular rate) is markedly improved by adaptively exploiting the coupling and disturbance.

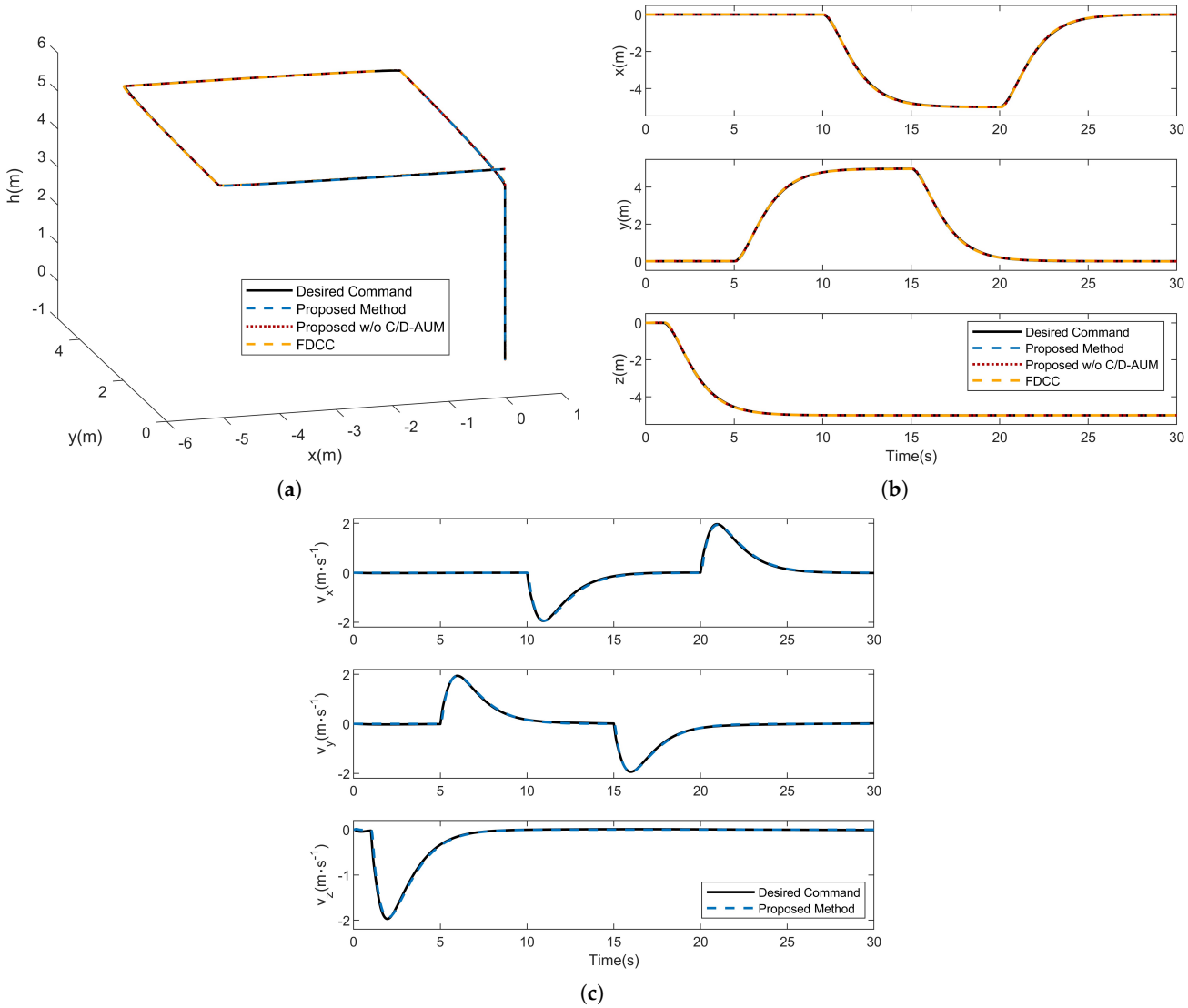


Figure 4. Three-dimensional position and velocity curves in comparative simulations. (**a**) Three-dimensional position tracking curves. (**b**) Three-axis position tracking curves. (**c**) Three-axis velocity tracking curves.

To provide a clearer and more quantitative performance comparison between the proposed method and the baseline methods, Tables 2–4 report the mean absolute error (MAE), root mean square error (RMSE), and mean bias error (MBE) obtained in the comparative simulations. These metrics characterize the tracking performance from two perspectives, namely, the average magnitude of the error (MAE and RMSE) and the bias property of the error distribution (MBE), thereby demonstrating the effectiveness of the proposed method. According to the MAE results summarized in Table 2, the proposed method achieves overall performance improvements of 39.27% and 31.97% compared with FDCC and the Proposed w/o C/D-AUM scheme, respectively. In addition, the RMSE and MBE results are consistently lower than those of the comparison methods. These results indicate that the proposed method improves both the dynamic performance and the steady-state performance. Additionally, Figure 10 shows the control input curves. Both the proposed

method and the comparison method maintain control inputs within reasonable ranges, validating their feasibility.

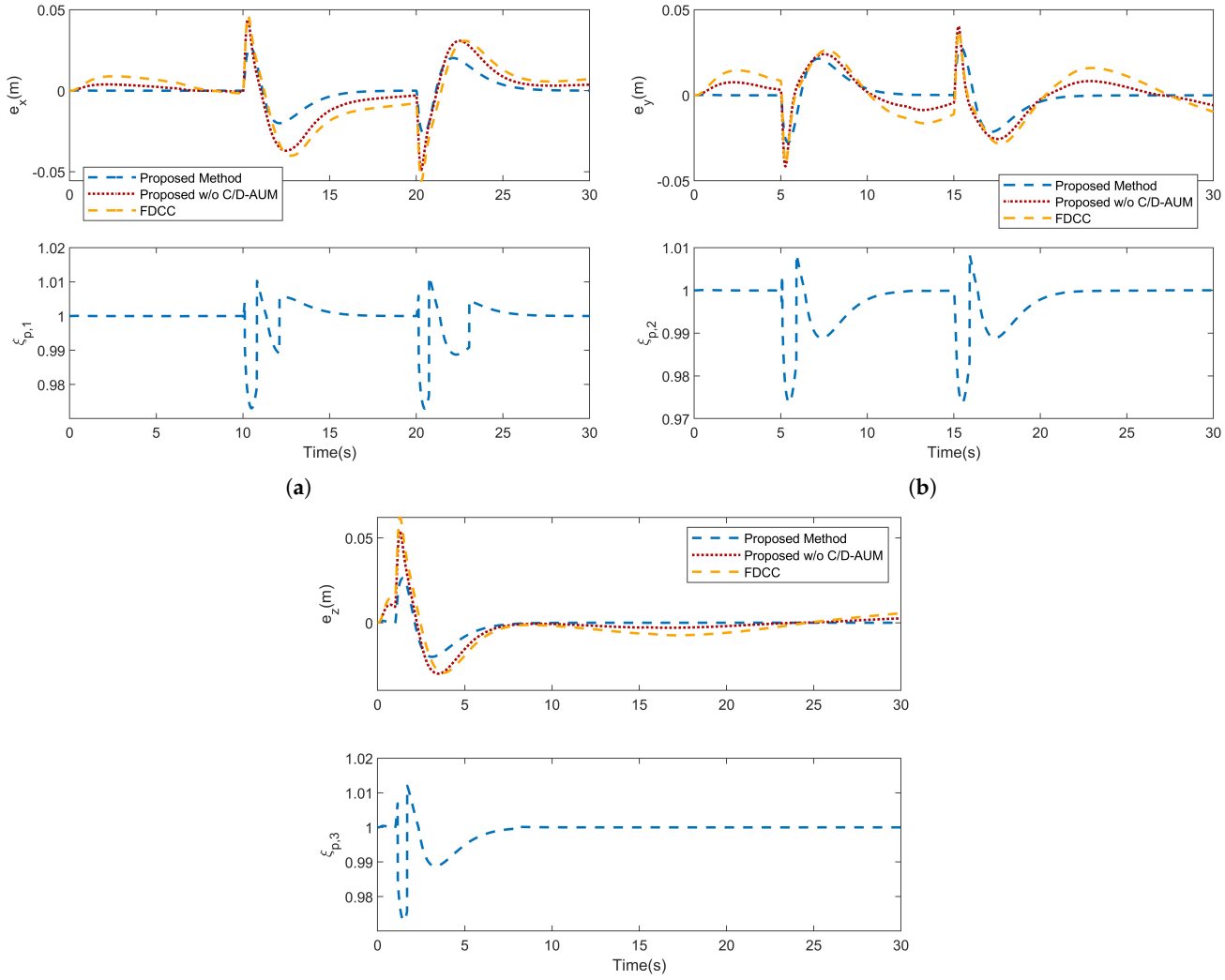


Figure 5. Three-axis position tracking errors and the outputs of C/D-AUM in comparative simulations. (**a**) x-axis position tracking error and C/D-AUM output $\xi_{p,1}$. (**b**) y-axis position tracking error and C/D-AUM output $\xi_{p,2}$. (**c**) z-axis position tracking error and $\xi_{p,3}$.

Table 2. MAE metrics in comparative simulations.

Channel	Proposed Method	Proposed w/o C/D-AUM	FDCC
x (m)	0.0047	0.0099	0.0131
y (m)	0.0050	0.0086	0.0122
z (m)	0.0024	0.0052	0.0075
v_x (m·s^{-1})	0.0181	0.0226	0.0190
v_y (m·s^{-1})	0.0162	0.0204	0.0189
v_z (m·s^{-1})	0.0104	0.0132	0.0113
ϕ (°)	0.0330	0.0415	0.0749
θ (°)	0.0324	0.0407	0.0591
ψ (°)	0.0349	0.0452	0.0811
p (°·s^{-1})	0.1654	0.2215	0.2167
q (°·s^{-1})	0.1636	0.2670	0.2247
r (°·s^{-1})	0.1274	0.2360	0.2281

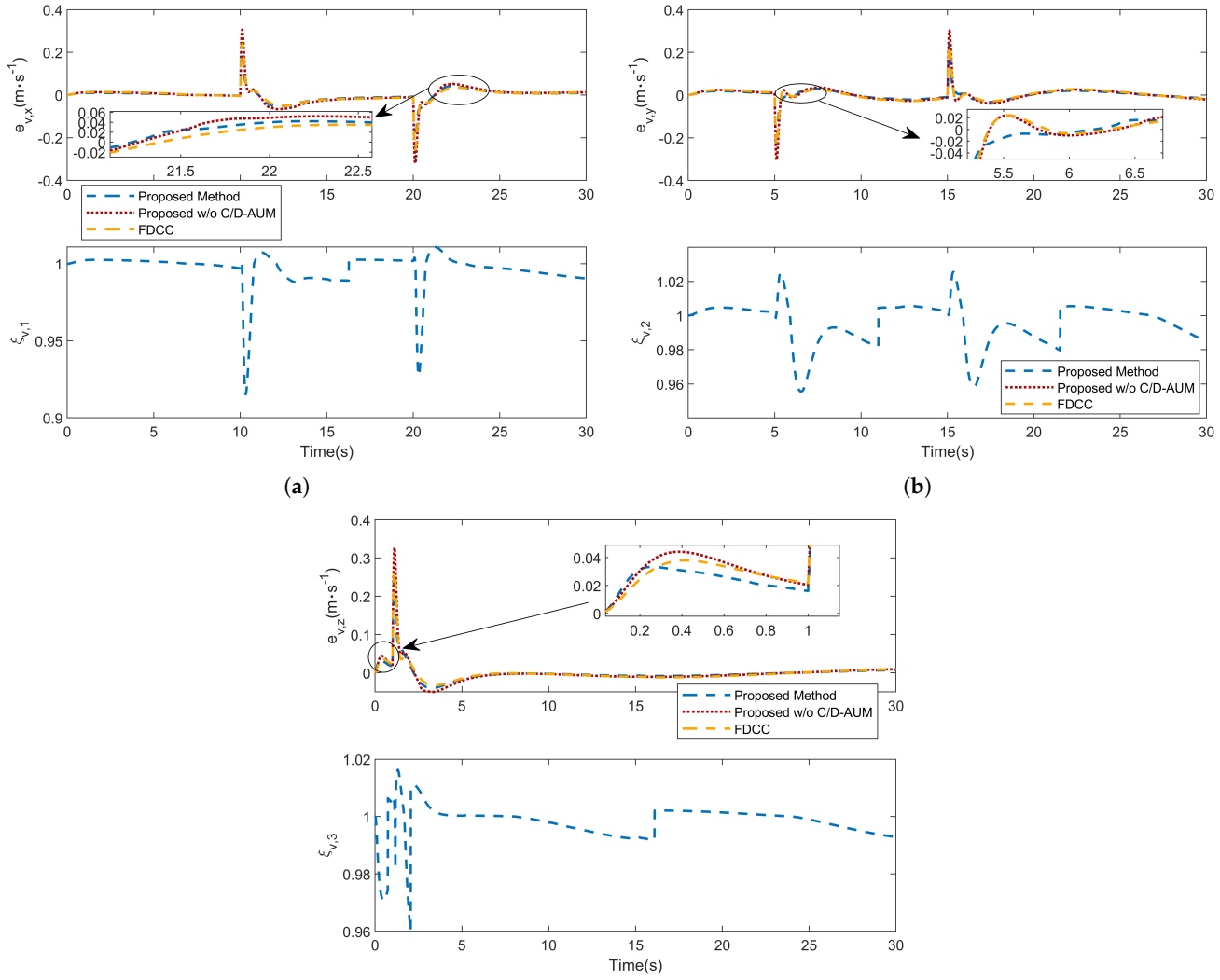


Figure 6. Three-axis velocity tracking errors and the outputs of C/D-AUM in comparative simulations. (**a**) x-axis velocity tracking error and C/D-AUM output $\xi_{v,1}$. (**b**) y-axis velocity tracking error and $\xi_{v,2}$. (**c**) z-axis velocity tracking error and $\xi_{v,3}$.

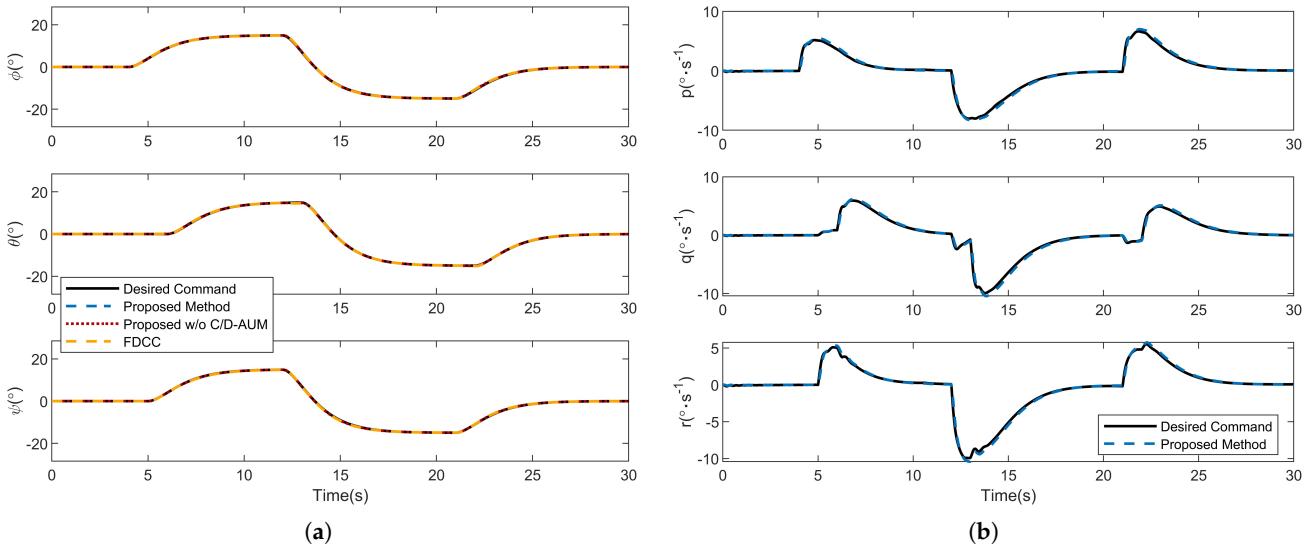


Figure 7. Three-axis angle and angular rate tracking curves in comparative simulations. (**a**) Three-axis angle tracking curves. (**b**) Three-axis angular rate tracking curves.

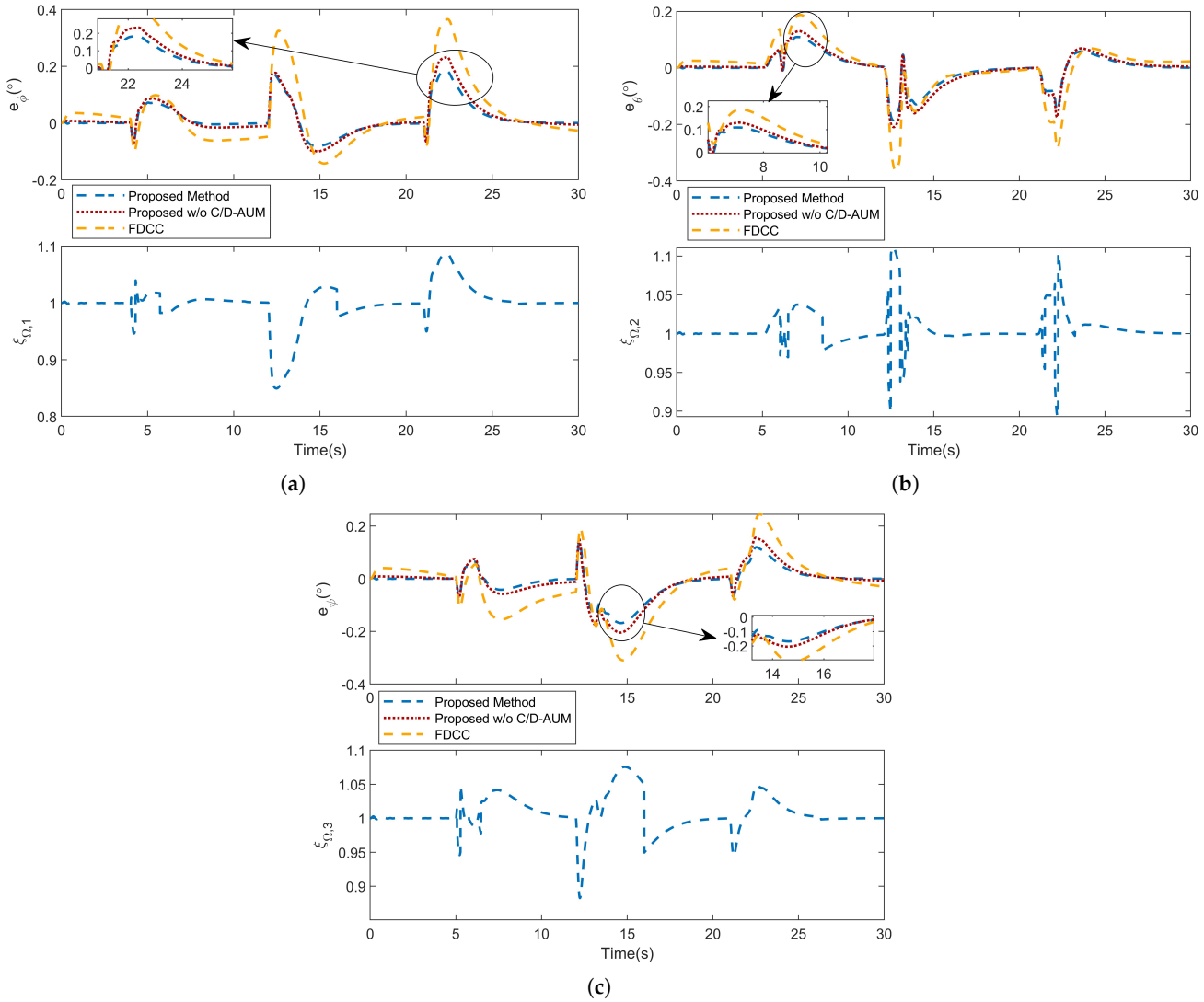


Figure 8. Three-axis angle tracking errors and the outputs of C/D-AUM in comparative simulations. (**a**) Roll angle tracking error and C/D-AUM output $\xi_{\Omega,1}$. (**b**) Pitch angle tracking error and $\xi_{\Omega,2}$. (**c**) Yaw angle tracking error and $\xi_{\Omega,3}$.

Table 3. RMSE metrics in comparative simulations.

Channel	Proposed Method	Proposed w/o C/D-AUM	FDCC
x (m)	0.0086	0.0149	0.0173
y (m)	0.0091	0.0117	0.0144
z (m)	0.0061	0.0102	0.0119
v_x (m·s^{-1})	0.0316	0.0406	0.0323
v_y (m·s^{-1})	0.0271	0.0360	0.0295
v_z (m·s^{-1})	0.0230	0.0295	0.0237
ϕ (°)	0.0564	0.0682	0.1138
θ (°)	0.0518	0.0627	0.0897
ψ (°)	0.0575	0.0712	0.1120
p (°·s^{-1})	0.2542	0.3172	0.2836
q (°·s^{-1})	0.2535	0.3943	0.3101
r (°·s^{-1})	0.2078	0.3518	0.3044

Table 4. MBE metrics in comparative simulations.

Channel	Proposed Method	Proposed w/o C/D-AUM	FDCC
x (m)	0.0000	−0.0008	−0.0007
y (m)	0.0000	0.0005	0.0014
z (m)	−0.0011	−0.0019	−0.0027
v_x (m·s^{-1})	−0.0009	−0.0012	−0.0009
v_y (m·s^{-1})	0.0012	0.0015	0.0019
v_z (m·s^{-1})	−0.0015	−0.0019	−0.0015
ϕ (°)	0.0160	0.0186	0.0295
θ (°)	−0.0014	−0.0020	0.0032
ψ (°)	−0.0122	−0.0144	−0.0268
p (°·s^{-1})	0.0240	0.0290	0.0193
q (°·s^{-1})	−0.0057	−0.0167	−0.0080
r (°·s^{-1})	−0.0015	−0.0025	0.0096

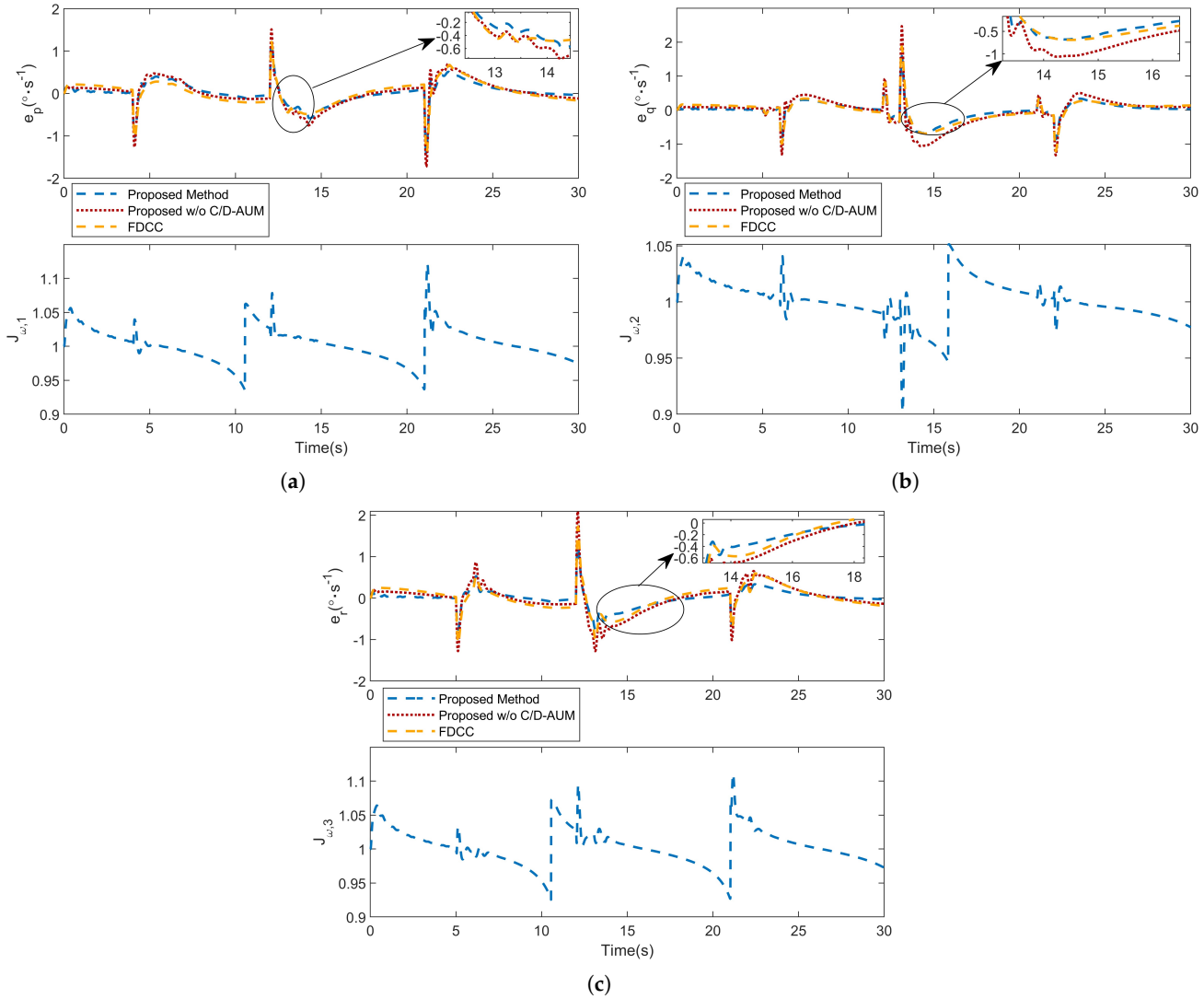
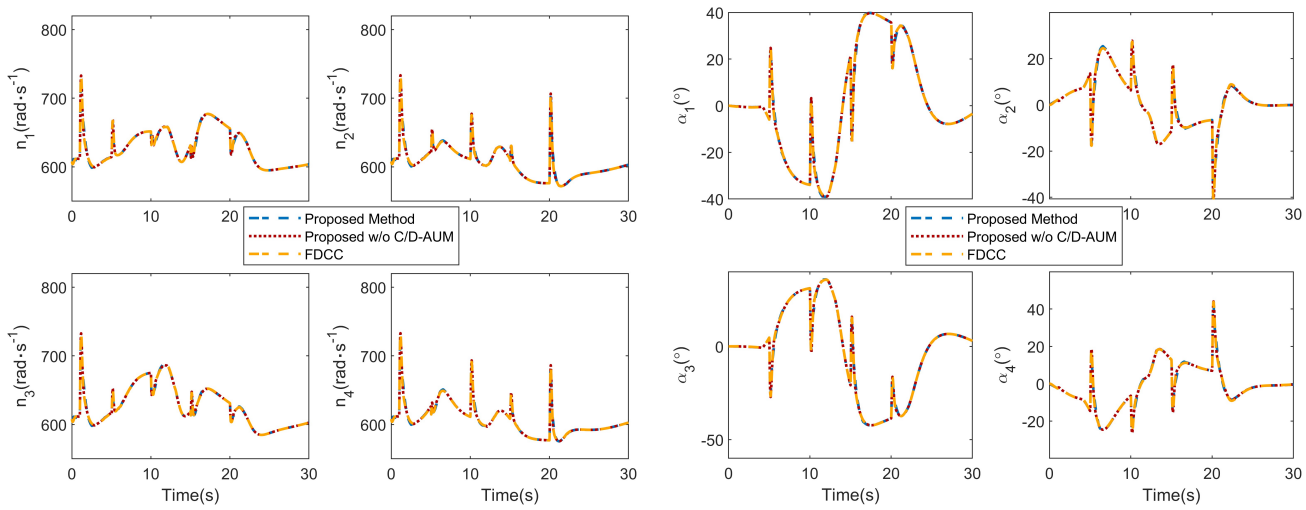


Figure 9. Three-axis angular rate tracking errors and the outputs of C/D-AUM in comparative simulations. (**a**) Roll angular rate tracking error and C/D-AUM output $\xi_{\omega,1}$. (**b**) Pitch angular rate tracking error and $\xi_{\omega,2}$. (**c**) Yaw angular rate tracking error and $\xi_{\omega,3}$.



(**a**) (**b**)

Figure 10. Control input curves in comparative simulations. (**a**) Rotor speed curves. (**b**) Servo tilt angle curves.

4.2. Monte Carlo Simulations

In this section, 300 Monte Carlo simulations are conducted under model parameter uncertainties, external disturbances, sensor noise, actuator dynamics, and communication delays, to further validate the robustness of the proposed method.

The Monte Carlo simulation settings are specified as follows. The reference commands for the position and attitude of the tiltable quadrotor are identical to those used in the comparative simulations. The model parameters are randomly perturbed within $\pm 20\%$. The disturbance coefficients k_{d_v} and k_{d_ω} are randomly varied within $[-2, 2]$. The control-input delay and the measurement/feedback delay are randomly selected within 1–3 control periods. Sensor noise is modeled as additive Gaussian noise. The $1-\sigma$ values for position, velocity, attitude angles, and angular rates are set to 0.01 m, 0.03 m/s, 0.1°, and 0.2°/s, respectively. The rotor speed and tilt angle dynamics are modeled as first-order inertial elements with a time constant of 0.02 s.

Figure 11 illustrates the position, velocity, attitude angle, and angular rate tracking error curves from a randomly selected Monte Carlo run, and Table 5 summarizes the statistical results of the MAE, RMSE, and MBE over 300 Monte Carlo simulations. As shown in Figure 11, incorporating practical factors of physical systems (e.g., sensor noise and time delays) inevitably increases the tracking errors. For the tiltable quadrotors, position and attitude accuracy are of primary concern. As shown in Figure 11a,c, the position and attitude angle errors can be maintained within ± 0.1 m and $\pm 0.5°$, respectively, indicating a high control precision. From the quantitative results in Table 5, it is evident that, despite the presence of noise, delays, and other practical factors, the proposed method still achieves satisfactory dynamic performance and steady state performance in terms of MAE, RMSE, and MBE. These results further corroborate the robustness of the proposed hierarchical adaptive coupling/disturbance utilization control method.

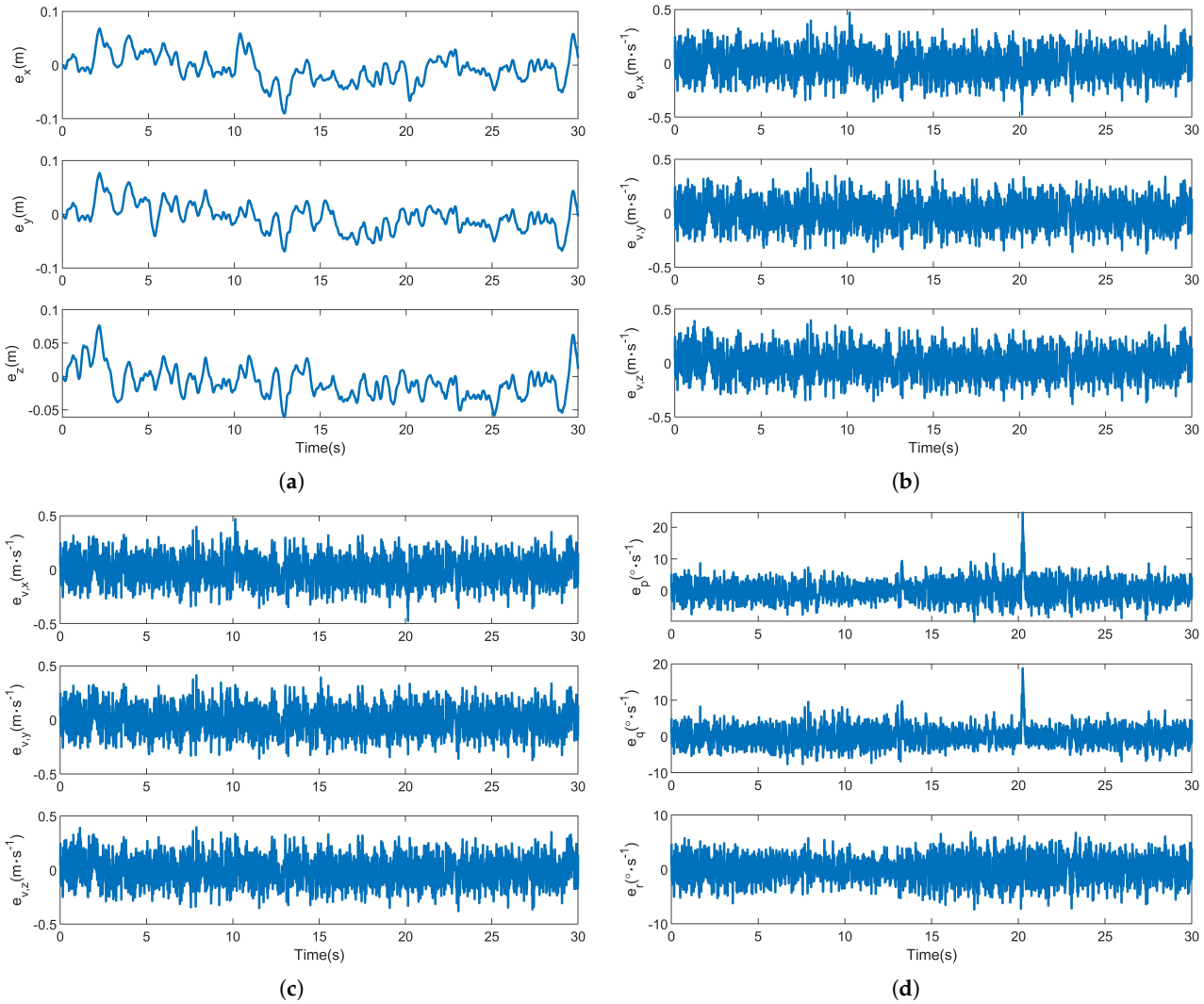


Figure 11. Tracking error curves in Monte Carlo simulations. (**a**) Position tracking errors. (**b**) Velocity tracking errors. (**c**) Attitude angle tracking errors. (**d**) Angular rate tracking errors.

Table 5. Performance metrics in Monte Carlo simulations.

Channel	MAE	RMSE	MBE
x (m)	0.0214	0.0272	−0.0066
y (m)	0.0203	0.0260	−0.0053
z (m)	0.0196	0.0244	−0.0089
v_x (m·s^{-1})	0.1005	0.1244	−0.0038
v_y (m·s^{-1})	0.1006	0.1245	−0.0026
v_z (m·s^{-1})	0.1012	0.1250	−0.0045
ϕ (°)	0.3285	0.5395	0.0138
θ (°)	0.3034	0.4723	0.0008
ψ (°)	0.1970	0.2497	−0.0179
p (°·s^{-1})	2.3696	3.0715	0.0852
q (°·s^{-1})	2.0009	2.5725	0.0959
r (°·s^{-1})	1.8496	2.2766	0.0606

5. Experimental Validation

In this section, the proposed method is validated through flight experiments. The hardware architecture of the tiltable quadrotor is shown in Figure 12.

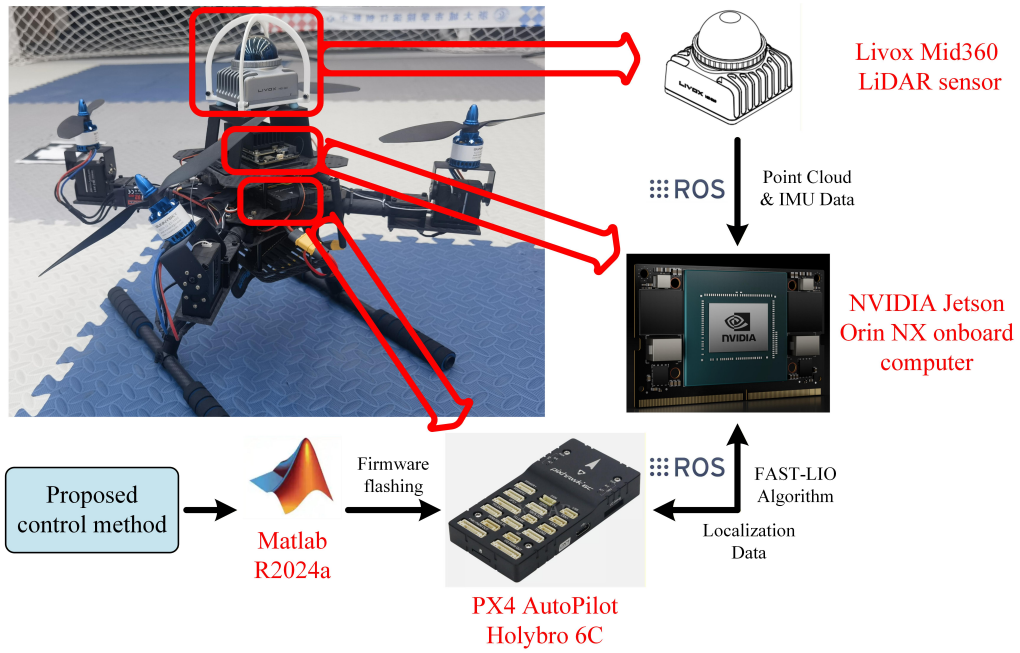


Figure 12. Hardware architecture of the tiltable quadrotor.

The flight experiment scenario is configured as follows. The tiltable quadrotor first takes off to an altitude of 1 m. It then hovers while the pitch and roll commands are varied within $\pm 20^\circ$. After that, the vehicle tracks a square reference trajectory with a side length of 2 m in the horizontal plane. Two fans are placed near the center of the square and operated in oscillating mode to generate a horizontal wind disturbance from varying directions, thereby emulating a 360° horizontal wind environment with a wind speed of approximately 3 m/s.

Figures 13 and 14 show the position and attitude angle tracking results from the flight experiment. Due to factors such as modeling errors, disturbances, and sensor noise, the control performance in the physical flight experiment is noticeably worse than the results obtained in the simulation. However, the proposed method still achieves excellent control performance. Additionally, since the rotor speed and servo tilt angles cannot be measured, the expected thrust and torque curves are presented in Figure 15 to validate the feasibility of the proposed method.

To provide a clearer quantitative performance comparison between the proposed method and the baseline methods, Tables 6–8 summarize the MAE, RMSE, and MBE obtained in the flight experiments. Since the proposed method incorporates the hierarchical C/D-AUM, it achieves improved tracking performance in both the outer loop and the inner loop, as indicated by the generally smaller MAE values. For the inner-loop performance, because both the proposed method and FDCC employ a disturbance-utilization mechanism, their MAE values are lower than those of the "Proposed w/o C/D-AUM" scheme for most channels. For the outer-loop performance, FDCC is slightly inferior to "Proposed w/o C/D-AUM" in a few cases, suggesting that disturbance utilization in the inner loop alone does not necessarily translate into improved outer-loop tracking accuracy. The RMSE and MBE results are also competitive among the three methods, with no obvious bias amplification observed. Overall, based on the averaged MAE across all reported channels, the proposed method achieves performance improvements of 12.18% and 24.49% compared with "Proposed w/o C/D-AUM" and FDCC, respectively.

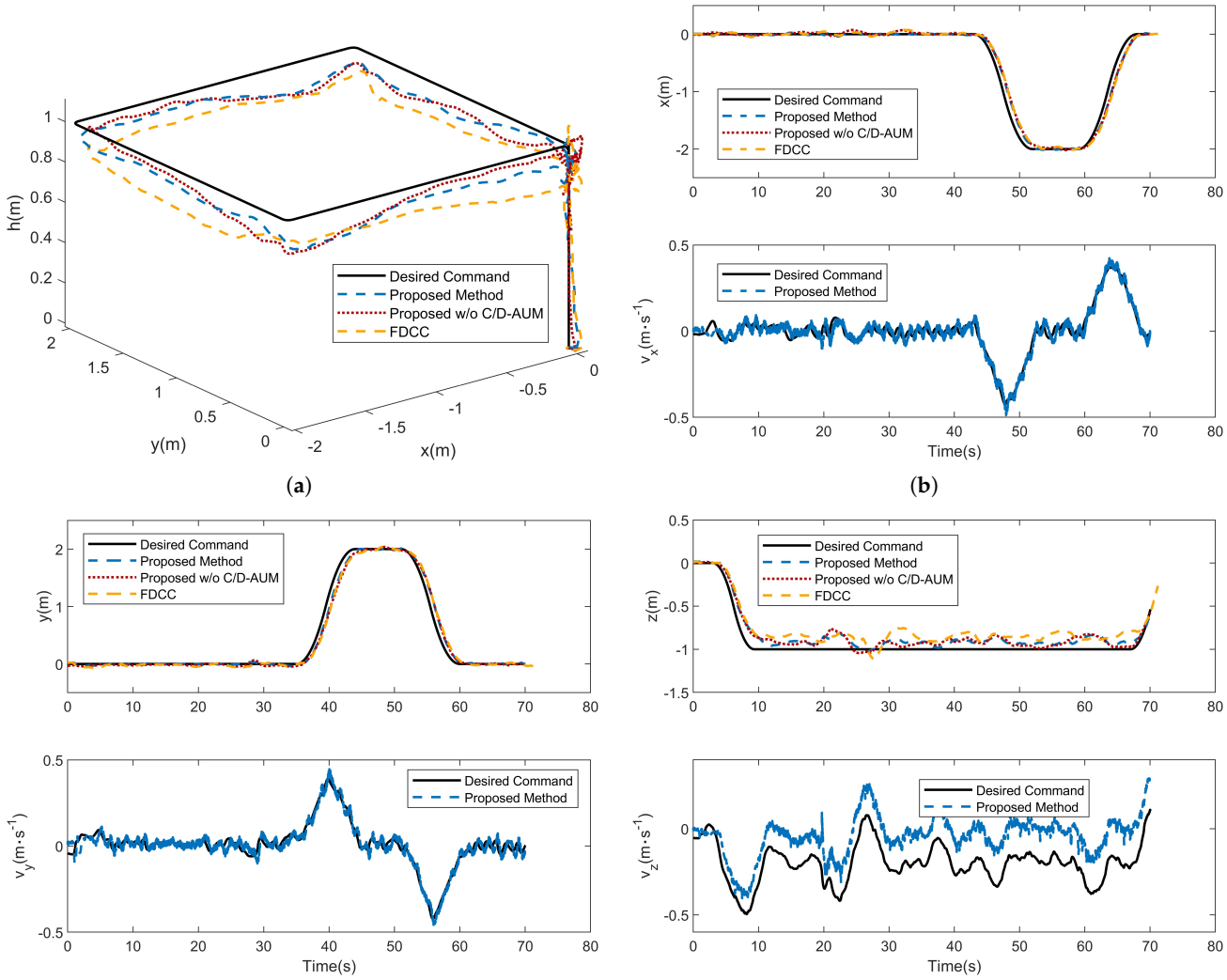


Figure 13. Three-dimensional position and velocity curves in the flight experiment results. (**a**) Three-dimensional trajectories. (**b**) x-axis position and velocity tracking curves. (**c**) y-axis position and velocity tracking curves. (**d**) z-axis position and velocity tracking curves.

Table 6. MAE metrics in experimental validation.

Channel	Proposed Method	Proposed w/o C/D-AUM	FDCC
x (m)	0.0464	0.0554	0.0575
y (m)	0.0444	0.0552	0.0596
z (m)	0.0784	0.0833	0.1384
v_x (m·s^{-1})	0.0237	0.0274	0.0256
v_y (m·s^{-1})	0.0249	0.0261	0.0255
v_z (m·s^{-1})	0.1455	0.1584	0.1720
ϕ (°)	0.7382	0.8876	0.8469
θ (°)	0.5291	0.5305	1.2145
p (°·s^{-1})	1.2439	1.4128	1.3529
q (°·s^{-1})	1.0349	1.2147	1.2827

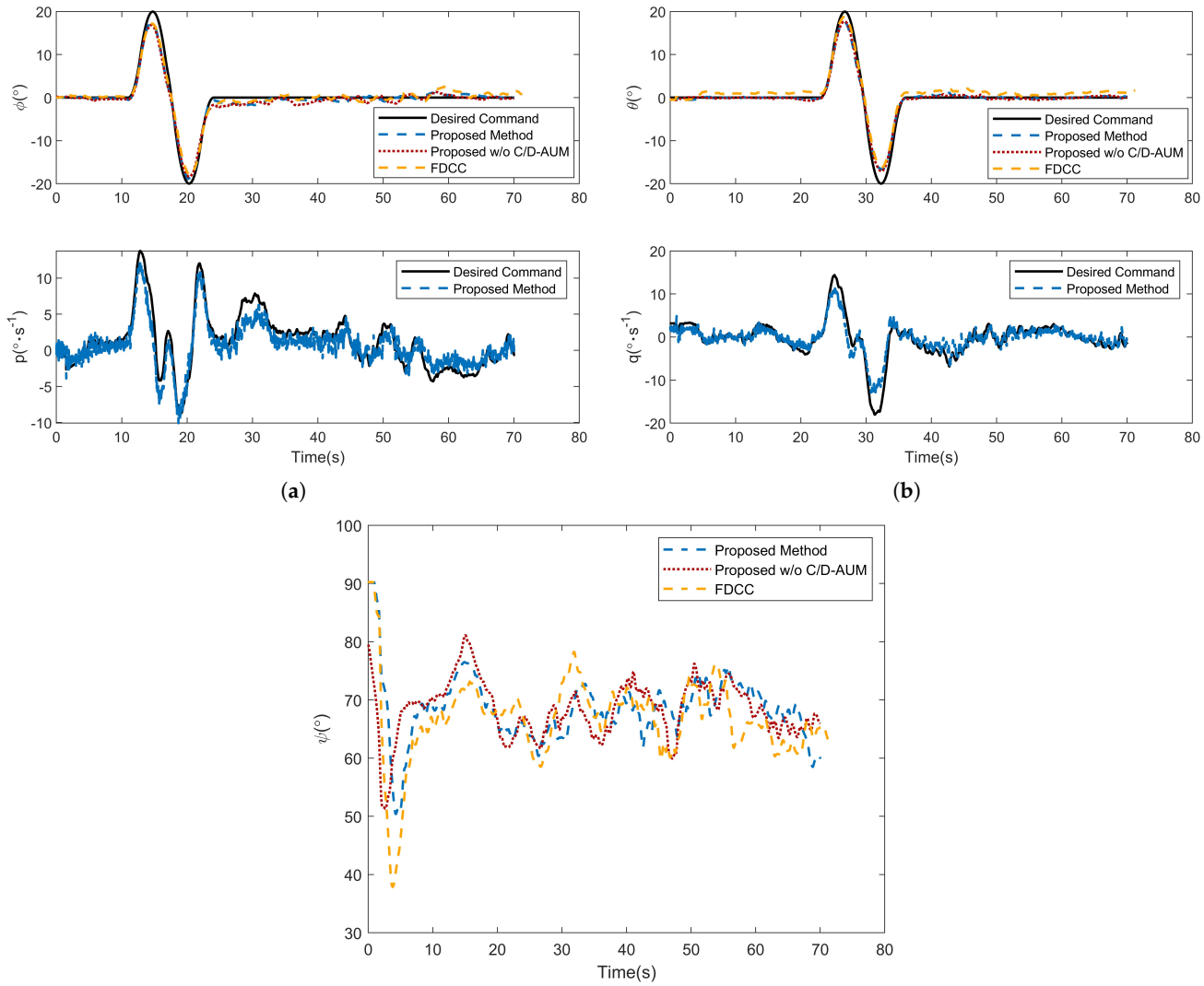


Figure 14. Three-axis angle and angular rate tracking curves in the flight experiment results. (**a**) Roll angle and angular rate tracking curves. (**b**) Pitch angle and angular rate tracking curves. (**c**) Yaw angle curves (In this paper, the yaw angle is controlled manually by the operator).

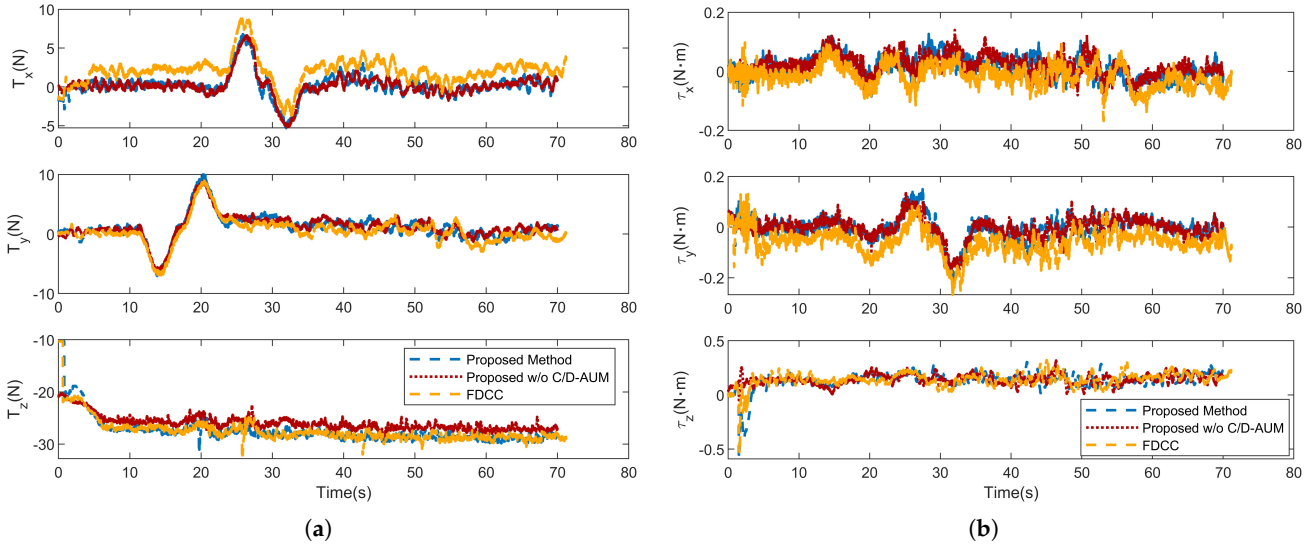


Figure 15. Three-axis thrust and torque curves in the flight experiment results. (**a**) Three-axis thrust curves. (**b**) Three-axis torque curves.

Table 7. RMSE metrics in experimental validation.

Channel	Proposed Method	Proposed w/o C/D-AUM	FDCC
x (m)	0.0876	0.0980	0.1013
y (m)	0.0829	0.0979	0.0996
z (m)	0.0967	0.1004	0.1501
v_x ($\mathrm{m{\cdot}s^{-1}}$)	0.0315	0.0335	0.0296
v_y ($\mathrm{m{\cdot}s^{-1}}$)	0.0308	0.0324	0.0319
v_z ($\mathrm{m{\cdot}s^{-1}}$)	0.1554	0.1644	0.2430
ϕ ($^\circ$)	1.0869	1.2805	1.1825
θ ($^\circ$)	0.9114	0.9339	1.4211
p ($^\circ{\cdot}\mathrm{s^{-1}}$)	1.5261	1.7269	1.7713
q ($^\circ{\cdot}\mathrm{s^{-1}}$)	1.4964	1.7170	2.7152

Table 8. MBE metrics in experimental validation.

Channel	Proposed Method	Proposed w/o C/D-AUM	FDCC
x (m)	0.0008	0.0137	0.0086
y (m)	−0.0046	−0.0146	−0.0140
z (m)	0.0785	0.0802	0.1334
v_x ($\mathrm{m{\cdot}s^{-1}}$)	0.0007	0.0199	0.0123
v_y ($\mathrm{m{\cdot}s^{-1}}$)	−0.0008	−0.0163	−0.0133
v_z ($\mathrm{m{\cdot}s^{-1}}$)	0.1168	0.1444	0.2314
ϕ ($^\circ$)	−0.1507	−0.5319	0.2330
θ ($^\circ$)	0.0095	−0.0260	1.0432
p ($^\circ{\cdot}\mathrm{s^{-1}}$)	−0.5346	−0.8281	0.6767
q ($^\circ{\cdot}\mathrm{s^{-1}}$)	0.0914	0.1071	0.1490

6. Conclusions

A hierarchical adaptive coupling/disturbance-utilization control framework is proposed to address the independent control problem of position and attitude. First, a control-oriented error dynamics model is developed, incorporating both inner–outer loop coupling and lumped disturbances, thus laying the foundation for the proposed framework. Then, hierarchical adaptive coupling/disturbance utilization mechanisms are designed, which enable the smooth exploitation of both beneficial couplings/disturbances and the advantageous effects of harmful ones. In addition, super-twisting sliding mode observers and robust tracking control laws are integrated into the overall control framework to guarantee the system's performance. Furthermore, the system's stability and the role of the utilization mechanisms are analyzed using Lyapunov methods. Simulation and flight experiments validate the effectiveness of the proposed method.

Combining the hierarchical adaptive coupling/disturbance utilization mechanism with optimal control methods to further enhance utilization efficiency and tracking performance is a future research direction.

Author Contributions: Conceptualization, T.W. and J.B.; methodology, T.W.; software, T.W.; validation, T.W.; formal analysis, T.W.; investigation, T.W. and J.B.; resources, J.B.; data curation, T.W.; writing—original draft preparation, T.W.; writing—review and editing, T.W., J.B. and M.X.; visualization, T.W.; supervision, J.B. and M.X.; project administration, T.W.; funding acquisition, J.B. All authors have read and agreed to the published version of the manuscript.

Funding: This work was supported by the National Key Research and Development Program of China under Grant No. 2023YFB3209800.

Data Availability Statement: Dataset available on request from the authors.

Acknowledgments: The authors would like to thank their colleagues at Hangzhou City University Binjiang Innovation Center, Shen Congqi (for assistance with mechanical structure design), Liu Zhen and Li Chenbin (for assistance with flight experiments), Hong Wei (for assistance with software development), and Long Chen (for assistance with indoor localization).

Conflicts of Interest: Author Min Xiong was employed by the company R&D Department, Jiangxi Jiangling Group Electric Vehicle Co., Ltd. The remaining authors declare that the research was conducted in the absence of any commercial or financial relationships that could be construed as a potential conflict of interest.

Abbreviations

The following abbreviations are used in this manuscript:

NMPC	Nonlinear Model Predictive Control
ESO	Extended State Observer
DO	Disturbance Observer
USDE	Unknown System Dynamics Estimator
ST-SMO	Super-twisting Sliding-mode Observer
C/D-AUM	Coupling/disturbance Adaptive Utilization Mechanism
RTC	Robust Tracking Control
FDCC	Flexible Disturbance Compensation Control

References

1. Sun, S.; Wang, X.; Sanalitro, D.; Franchi, A.; Tognon, M.; Alonso-Mora, J. Agile and Cooperative Aerial Manipulation of a Cable-Suspended Load. *Sci. Robot.* **2025**, *10*, eadu8015. [CrossRef] [PubMed]
2. Saviolo, A.; Loianno, G. Learning Quadrotor Dynamics for Precise, Safe, and Agile Flight Control. *Annu. Rev. Control* **2023**, *55*, 45–60. [CrossRef]
3. Montoya-Morales, J.; Guerrero-Sánchez, M.; Valencia-Palomo, G.; Hernández-González, O.; López-Estrada, F.; Hoyo-Montaño, J. Real-Time Robust Tracking Control for a Quadrotor Using Monocular Vision. *Proc. Inst. Mech. Eng. Part G J. Aerosp. Eng.* **2023**, *237*, 2729–2741. [CrossRef]
4. Durán-Delfín, J.E.; García-Beltrán, C.D.; Guerrero-Sánchez, M.E.; Valencia-Palomo, G.; Hernández-González, O. Modeling and Passivity-Based Control for a Convertible Fixed-Wing VTOL. *Appl. Math. Comput.* **2024**, *461*, 128298. [CrossRef]
5. Zhao, C.; Wang, E.; Guo, K.; Yu, X. Design and Antidisturbance Control for an H-Configuration Tiltable QuadRotor: Enabling Narrow Space Crossing. *IEEE Trans. Aerosp. Electron. Syst.* **2024**, *60*, 4452–4462. [CrossRef]
6. Nemati, A.; Kumar, M. Modeling and Control of a Single Axis Tilting Quadcopter. In Proceedings of the 2014 American Control Conference, Portland, OR, USA, 4–6 June 2014; pp. 3077–3082. [CrossRef]
7. Ryll, M.; Bulthoff, H.H.; Giordano, P.R. A Novel Overactuated Quadrotor Unmanned Aerial Vehicle: Modeling, Control, and Experimental Validation. *IEEE Trans. Contr. Syst. Technol.* **2015**, *23*, 540–556. [CrossRef]
8. Xing, S.; Zhang, X.; Tian, J.; Xie, C.; Chen, Z.; Sun, J. Morphing Quadrotors: Enhancing Versatility and Adaptability in Drone Applications—A Review. *Drones* **2024**, *8*, 762. [CrossRef]
9. Ozdogan, G.; Leblebicioglu, K. Design, Modeling, and Control Allocation of a Heavy-Lift Aerial Vehicle Consisting of Large Fixed Rotors and Small Tiltrotors. *IEEE/ASME Trans. Mechatron.* **2022**, *27*, 4011–4021. [CrossRef]
10. Saif, A.W.A.; Aliyu, A.; Dhaifallah, M.A.; Elshafei, M. Decentralized Backstepping Control of a Quadrotor with Tilted-rotor under Wind Gusts. *Int. J. Control Autom. Syst.* **2018**, *16*, 2458–2472. [CrossRef]
11. Shayan, Z.; Cristobal, J.; Izadi, M.; Yazdanshenas, A.; Naderi, M.; Faieghi, R. Nonlinear Model Predictive Control of Tiltrotor Quadrotors Using Feasible Control Allocation. *J. Intell. Robot. Syst.* **2025**, *111*, 54. [CrossRef]
12. Li, J.; Sugihara, J.; Zhao, M. Servo Integrated Nonlinear Model Predictive Control for Overactuated Tiltable-Quadrotors. *IEEE Robot. Autom. Lett.* **2024**, *9*, 8770–8777. [CrossRef]
13. Yang, Y.; Yu, X.; Li, Z.; Basin, M.V. A New Overactuated Multirotor: Prototype Design, Dynamics Modeling, and Control. *IEEE Trans. Ind. Electron.* **2024**, *71*, 9449–9459. [CrossRef]
14. He, J.; Ren, B.; Xu, Y.; Zhao, Q.; Du, S.; Wang, B. Neural Network Adaptive Attitude Control of Full-States Quad Tiltrotor UAV. *Aerospace* **2025**, *12*, 684. [CrossRef]
15. Xiong, J.J.; Wang, X.Y.; Li, C. Recurrent Neural Network Based Sliding Mode Control for an Uncertain Tilting Quadrotor UAV. *Int. J. Robust Nonlinear Control* **2025**, *35*, 8030–8046. [CrossRef]

16. Xie, Y.; Yu, X.; Qiao, J.; Zhang, K.; Shi, Y.; Guo, L. Composite Anti-Disturbance Control with Disturbance Prediction and Utilization: A Tube MPC Approach. *Automatica* **2026**, *184*, 112700. [CrossRef]
17. Sun, J.; Xu, S.; Ding, S.; Pu, Z.; Yi, J. Adaptive Conditional Disturbance Negation-Based Nonsmooth-Integral Control for PMSM Drive System. *IEEE/ASME Trans. Mechatron.* **2024**, *29*, 3602–3613. [CrossRef]
18. Teng, H.; Lu, Y.; Xia, P.; Qiao, J.; Guo, L. Refined Disturbance Utilization-Based Green Control for Spacecraft With Composite Actuator Disturbances. *IEEE/ASME Trans. Mechatron.* **2025**, *30*, 5652–5662. [CrossRef]
19. Zhao, Z.; Wang, G.; Ma, G.; Xia, H. Resilient Predefined-Time Neuroadaptive Control for Spacecraft Formation: Conditional Compensation and Hierarchical Learning. *IEEE Trans. Aerosp. Electron. Syst.* **2025**, *62*, 1275–1292. [CrossRef]
20. Fang, X.; Ruan, Z.; Zhao, S.; Liu, F. Conditional Disturbance-Compensation Control for an Overactuated Manned Submersible Vehicle. *IEEE Trans. Ind. Inf.* **2024**, *20*, 4828–4838. [CrossRef]
21. Sun, J.; Pu, Z.; Chang, Y.; Ding, S.; Yi, J. Appointed-Time Control for Flexible Hypersonic Vehicles with Conditional Disturbance Negation. *IEEE Trans. Aerosp. Electron. Syst.* **2023**, *59*, 6327–6345. [CrossRef]
22. Sun, J.; Pu, Z.; Yi, J. Conditional Disturbance Negation Based Active Disturbance Rejection Control for Hypersonic Vehicles. *Control Eng. Pract.* **2019**, *84*, 159–171. [CrossRef]
23. Guo, Z.; Ma, Q.; Guo, J.; Zhao, B.; Zhou, J. Performance-Involved Coupling Effect-Triggered Scheme for Robust Attitude Control of HRV. *IEEE/ASME Trans. Mechatron.* **2020**, *25*, 1288–1298. [CrossRef]
24. Wu, T.; Bai, J.; Shi, Z.; Jiang, H. Flexible Disturbance-Compensation Control for Tiltable Quadrotors Considering Input Constraints. *Appl. Math. Model.* **2026**, *153*, 116653. [CrossRef]
25. Guo, Z.; Yao, L.; Cao, S.; Ding, Y.; Yuan, R.; Huang, L.; Guo, J. Integrated Missile Guidance and Control Scheme via Coupling Effect Utilization and Transformation Mechanism. *IEEE Trans. Aerosp. Electron. Syst.* **2025**, *61*, 2068–2077. [CrossRef]
26. Guo, Z.; Zhou, J.; Guo, J.; Cieslak, J.; Chang, J. Coupling-Characterization-Based Robust Attitude Control Scheme for Hypersonic Vehicles. *IEEE Trans. Ind. Electron.* **2017**, *64*, 6350–6361. [CrossRef]
27. Li, Z.; Yang, Y.; Yu, X.; Liu, C.; Kaynak, O.; Gao, H. Fixed-Time Control of a Novel Thrust-Vectoring Aerial Manipulator via High-Order Fully Actuated System Approach. *IEEE/ASME Trans. Mechatron.* **2025**, *30*, 1084–1095. [CrossRef]
28. Smith, S.; Pan, Y.J. Adaptive Observer-Based Super-Twisting Sliding Mode Control for Low Altitude Quadcopter Grasping. *IEEE/ASME Trans. Mechatron.* **2025**, *30*, 587–598. [CrossRef]
29. Liu, Y.C.; Laghrouche, S.; Depernet, D.; Djerdir, A.; Cirrincione, M. Disturbance-Observer-Based Complementary Sliding-Mode Speed Control for PMSM Drives: A Super-Twisting Sliding-Mode Observer-Based Approach. *IEEE J. Emerg. Sel. Topics Power Electron.* **2021**, *9*, 5416–5428. [CrossRef]
30. Guo, Z.; Guo, J.; Zhou, J.; Chang, J. Robust Tracking for Hypersonic Reentry Vehicles via Disturbance Estimation-Triggered Control. *IEEE Trans. Aerosp. Electron. Syst.* **2020**, *56*, 1279–1289. [CrossRef]
31. Kong, S.; Sun, J.; Wang, J.; Zhou, Z.; Shao, J.; Yu, J. Piecewise Compensation Model Predictive Governor Combined With Conditional Disturbance Negation for Underactuated AUV Tracking Control. *IEEE Trans. Ind. Electron.* **2023**, *70*, 6191–6200. [CrossRef]

Disclaimer/Publisher's Note: The statements, opinions and data contained in all publications are solely those of the individual author(s) and contributor(s) and not of MDPI and/or the editor(s). MDPI and/or the editor(s) disclaim responsibility for any injury to people or property resulting from any ideas, methods, instructions or products referred to in the content.